

RESHOCK GAS CURTAIN MIXING STUDY

A Thesis
Presented to
The Academic Faculty

By

Karl Risley

In Partial Fulfillment
of the Requirements for the Degree
Master's in Aerospace Engineering in the
Daniel Guggenheim School of Aerospace Engineering
Computational Combustion Lab

Georgia Institute of Technology

August 2022

RESHOCK GAS CURTAIN MIXING STUDY

Thesis committee:

Dr. Suresh Menon
Aerospace Engineering
Georgia Institute of Technology

Dr. Devesh Ranjan
Mechanical Engineering
Georgia Institute of Technology

Dr. Joseph Oefelein
Aerospace Engineering
Georgia Institute of Technology

Date approved: April 11, 2022

ACKNOWLEDGMENTS

This work would not have been possible without the funding from the Defense Threat Reduction Agency. I am extremely grateful for the experiences I have had in the Computational Combustion Lab thus far. I have had the opportunity to work with very intelligent and wonderful people who have pushed me to become a better engineer. To say I have learned a lot from these experiences would be an understatement. First and foremost, I would like to thank my advisor Dr. Suresh Menon for constantly challenging me and providing me the opportunity to pursue the research presented in this proposal. Additionally, I would like to thank Pavan Patel, a fellow GRA and friend, for his willing input into my work that also made this work possible. I am very thankful for the support of my family through this process as well. Lastly, I would like to thank my wife, Emily, for all that she has done to support me in this season. I could never repay the sacrifices that she has selflessly made and I am forever grateful.

SUMMARY

The current work investigates the behavior of gas curtain instabilities. A gas curtain can be visualized as an $A \mid B \mid A$ domain, where A and B are light and heavy fluids respectively, creating a "curtain" of heavy fluid B that is surrounded by a light fluid A . Specifically, the behavior of gas curtains following an initial shock passage and the passage of a reflected shock (reshock) through the entirety of the curtain are investigated. A gas curtain instability commonly occurs physically in a wide range of applications such as during afterburning of an explosion, inertial confinement fusion, and even supernovae explosions. Previous studies have emphasized that the physics occurring during the reshock of a gas curtain are far more complex than the behavior of a re-shock Richtmyer-Meshkov Instability, due to the interactions between the two interfaces and wave reverberations occurring. The current work attempts to understand the relationship between a gas curtain's initial conditions and its behavior to reshock through two-dimensional numerical simulations that utilize the viscous Navier-Stokes equations. More specifically, the current work isolates the effects of the curtain's initial thickness and shape on the post reshock mixing layer growth rate and molecular mixing of the curtain. The results for all cases indicate that the post-reshock growth rate of the curtain's width is a function of initial thickness. The sensitivity of the curtain's post-reshock growth rate to the initial thickness, however, depends on the curtain's initial perturbation shape. As the initial thickness of the curtain is decreased, the interactions between the curtain's interfaces grow in strength and impede perturbation growth, thus reducing the post reshock growth rate of the curtain's structure width. Similarly, the results strongly suggest that a reduction in initial curtain thickness increases the late-time asymptotic molecular mixing fraction value. This result is significant, especially for reacting flows, because it indicates that faster combustion (or afterburning in an explosion) could be reached with the thinning of the gas curtain in flow systems.

TABLE OF CONTENTS

| | |
|---|------|
| Acknowledgments | iii |
| Summary | iv |
| List of Tables | viii |
| List of Figures | x |
| List of Acronyms | xiii |
| Chapter 1: Introduction and Background | 1 |
| 1.1 Introduction | 1 |
| Chapter 2: Literature Review and Background | 5 |
| 2.1 Richtmyer Meshkov Instability | 5 |
| 2.1.1 Pre-Reshock RMI Growth Rate | 7 |
| 2.1.2 Reshock RMI Growth Rate | 10 |
| 2.2 Previous Curtain Studies | 13 |
| 2.3 Previous Reshock Curtain Studies | 22 |
| Chapter 3: Objectives | 25 |
| Chapter 4: Simulation Methodology and Set-Up | 28 |

| | | |
|--|--|-----------|
| 4.1 | Simulation Methodology | 28 |
| 4.2 | Numerical Formulation | 31 |
| 4.2.1 | Finite Volume Method | 32 |
| 4.2.2 | Time Integration - MacCormack Scheme | 32 |
| 4.2.3 | Central Schemes | 33 |
| 4.2.4 | Flux Difference Splitting Method | 33 |
| 4.3 | Mixing Quantification | 34 |
| 4.3.1 | Mixing Length | 34 |
| 4.3.2 | Gas Curtain Width Calculation | 35 |
| 4.4 | Molecular Mixing Calculation | 37 |
| 4.5 | Domain Definition | 38 |
| 4.5.1 | Supersonic Inflow | 39 |
| 4.5.2 | Periodic BC | 39 |
| 4.5.3 | Closed Wall | 40 |
| 4.6 | Grid Definition and Sensitivity Study | 40 |
| Chapter 5: Verification | | 42 |
| 5.1 | Single Interface RMI | 42 |
| 5.2 | Reference Cases | 45 |
| 5.2.1 | Balakumar <i>et al.</i> Case Definition [8] | 45 |
| 5.2.2 | Balasubramanian <i>et al.</i> Case Definition [31] | 51 |
| Chapter 6: Results and Discussion | | 54 |
| 6.1 | Single Shock Studies | 57 |

| | | |
|---|---|-----------|
| 6.1.1 | Single Mode Shape Study | 57 |
| 6.1.2 | Single Mode Curtain Thickness Study | 63 |
| 6.1.3 | Multi-Mode Shape Study | 72 |
| 6.1.4 | Multi-Mode Curtain Thickness Study | 76 |
| 6.2 | Reshock Studies | 77 |
| 6.2.1 | Single Mode Shape Reshock Studies | 77 |
| 6.2.2 | Single Mode Curtain Thickness Reshock Studies | 79 |
| 6.2.3 | Multi-Mode Curtain Reshock Studies | 84 |
| 6.2.4 | Multi-Mode Curtain Thickness Reshock Studies | 88 |
| 6.2.5 | Effect of Random Fluctuations | 90 |
| 6.3 | Discussion of Applicability | 91 |
| Chapter 7: Conclusions | | 93 |
| 7.1 | Summary | 93 |
| 7.2 | Future Work | 94 |
| References | | 96 |

LIST OF TABLES

| | | |
|-----|---|----|
| 2.1 | Coefficients for Theoretical Models. | 9 |
| 4.1 | Grid Sensitivity Study. | 40 |
| 5.1 | Verification Case Initial Conditions $M_s = 1.2$ | 43 |
| 5.2 | Verification Case Interface Initial Geometry. | 43 |
| 5.3 | Shankar and Lele tested Initial Peak Mass Fractions for Acetone and SF_6 [7]. | 47 |
| 5.4 | Current Work tested Initial Peak Mass Fractions for Acetone and SF_6 | 49 |
| 5.5 | Experimental initial conditions sourced from [31] that vary initial curtain shape. | 51 |
| 5.6 | Scaled Parameters to mathematically represent the initial conditions presented in Table 5.5. Note that only the wavenumbers differ between cases. . . | 52 |
| 6.1 | Single Mode Shape Study Test Cases. | 57 |
| 6.2 | redSingle Mode Shape Study Test Cases. | 57 |
| 6.3 | Single Mode Amplitude Study Test Cases. | 59 |
| 6.4 | Single Mode Curtain Thickness Study Test Cases. | 64 |
| 6.5 | Characterization Methods for Gas Curtain Instabilities. | 69 |
| 6.6 | Comparison of Mikaelian’s Model [17] and the current work’s simulation results for the amplitude growth rate of the upstream interface. | 71 |
| 6.7 | Multi-Mode Curtain Shape Study Test Cases. | 72 |

| | | |
|------|---|----|
| 6.8 | Multi-Mode Curtain Thickness Study Test Cases. | 76 |
| 6.9 | Reshock Parameters for Single-Mode Shape Studies. | 78 |
| 6.10 | Additional Single Mode Thickness Study Test Cases. | 80 |
| 6.11 | [9]'s characterization applied to multi-modal gas curtains. | 85 |
| 6.12 | Multi-Mode Thin Curtain Definitions. | 86 |

LIST OF FIGURES

| | | |
|-----|---|----|
| 1.1 | RMI Schematic sourced from [3]. | 2 |
| 1.2 | Basic Schematic of Gas Curtain. | 3 |
| 2.1 | Misalignment of Pressure and Density Gradients Over Contact Interface. Sourced from [9]. | 6 |
| 2.2 | Bubble and Spike Definitions, sourced from [9]. | 6 |
| 2.3 | Flow Patterns observed during the shock acceleration of a Gas Curtain, sourced from [30]. | 15 |
| 4.1 | Difference between Iso-Contour and Threshold Mixing Length Definition [20]. | 36 |
| 4.2 | Domain Definition Schematic sourced from [3]. | 38 |
| 4.3 | Grid Sensitivity of 2D single-mode gas curtain Structure Width W compu- tations. | 41 |
| 5.1 | Verification Case Initial Conditions. Initial interface pictured without dif- fusion modelled. | 43 |
| 5.2 | Comparison with 2D Empirical Models and Ukai et al. [9]. Mixing Length is normalized by first subtracting the post-shock mixing length, and then dividing this difference by the initial mixing length. | 44 |
| 5.3 | Experimental Shock Tube used by Balakumar <i>et al.</i> [8] | 45 |
| 5.4 | Experimental Nozzle used by Balakumar <i>et al.</i> [8] | 46 |

| | | |
|-----|--|----|
| 5.5 | Visualization of initial heavy gas mass distribution used by the current work to numerically reproduce the experimental findings of Balakumar <i>et al.</i> [8], viewed normal to the z-axis. Note that the grid lines merely provide further visualization of the curtain’s geometry and do not represent the computational grid. | 49 |
| 5.6 | Current Simulation Results for Curtain Width, compared to available experimental [8] and numerical data [7, 4]. Curtain width is plotted as difference between the curtain width values and the post-shock curtain width W_0^+ | 50 |
| 5.7 | Visualization of initial SF_6 gas mass distribution for Case SM-1 and SM-2, respectively, viewed normal to the z-axis. Note that the grid lines merely provide further visualization of the curtain’s geometry and do not represent the computational grid. | 52 |
| 5.8 | Current Simulation Results for SM-1 and SM-2 Curtain Width, compared to available experimental data [31]. Curtain width is plotted as difference between the curtain width values and the initial curtain width W_0 | 53 |
| 6.1 | Basic Schematic of Simulation Domain. | 54 |
| 6.2 | Initial Conditions Visualization for Case SM-a. Note that the grid lines merely provide further visualization of the curtain’s geometry and do not represent the computational grid. | 56 |
| 6.3 | Single Mode Gas Curtain Growth Results, structure width and time are normalized by their respective value immediately following shock passage ($t_0^+; W_0^+$). | 58 |
| 6.4 | Variation of initial amplitude effect on gas curtain instabilities. | 59 |
| 6.5 | Single Mode Molecular Fraction Results for Cases defined in Table 6.2. | 61 |
| 6.6 | Contour Plots of SF_6 mass fraction for case SM-C, used to visualize the molecular diffusion occurring across the upstream interface before shock passage (shock reaches curtain upstream interface at approximately 140 s. From left to right: $t = 0$ s, $t = 40$ s, $t = 140$ s. | 62 |
| 6.7 | Gas curtain growth (a) and (b) results for Cases defined in Table 6.4. In (a) $t = 0$ s corresponds to immediately after shock passage. In (b) $t = 200$ s corresponds to immediately after shock passage. | 64 |
| 6.8 | Contour plots of ρ_z for cases SM-A and SM-G at times after initial shock passage (t_0^+). | 66 |

| | | |
|------|--|----|
| 6.9 | Contour plots of θ_z for cases SM-G at times after initial shock passage (t_0^+). | 68 |
| 6.10 | Contour plots of Y_{SF_6} for cases SM-G and SM-A. | 69 |
| 6.11 | Contour plots of Y_{SF_6} for cases A' (RMI) and the upstream interface of SM-H (Thick Curtain). Notice that the development of the instabilities are indistinguishable, showing that at sufficiently large curtain thicknesses, the single-interface RMI behavior is recovered. | 70 |
| 6.12 | Multi-mode gas curtain growth (a) results and (b) for cases differing in initial number of modes. | 73 |
| 6.13 | Contour plots of $\frac{kg}{m^3}$ for cases MM-2 (TOP) and MM-8 (Bottom). | 75 |
| 6.14 | Multi-mode gas curtain growth (a) results and (b) for cases differing in initial thickness. | 76 |
| 6.15 | Single Mode Gas Curtain Post-Reshock Growth Results and for cases differing in initial shapes (θ_0 and a_0) (Table 6.2). | 78 |
| 6.16 | Gas Curtain Post-Reshock Growth and Results for cases differing in initial thickness (Table 6.4). | 79 |
| 6.17 | Single-Mode Curtain Thickness Study for large-wavelength curtains defined in Table 6.10. | 81 |
| 6.18 | Contour plots of $\theta_z \frac{rad}{s}$ for cases SM-7-6 (TOP) and SM-7-1 (Bottom) after initial shock passage. | 82 |
| 6.19 | Contour plots of SF_6 for cases SM-7-6 (TOP) and SM-7-1 (Bottom) after initial shock passage. | 83 |
| 6.20 | Multi-Mode Gas Curtain Post-Reshock Growth and Results for cases differing in shape (Equation 6.2). | 84 |
| 6.21 | Contour plots of Y_{SF_6} for cases MM-2 (TOP) and MM-8 (Bottom) after reshock. | 85 |
| 6.22 | Structure Width versus time for Cases defined in Table 6.12. | 87 |
| 6.23 | Contour plots of Y_{SF_6} for cases MM-2-1 (TOP) and MM-8-1 (Bottom) after reshock. t_R^+ represents time after reshock. | 88 |

| | |
|--|----|
| 6.24 Multi-Mode Gas Curtain Post-Reshock Growth for (a) MM-2 and (b) MM-8 cases. | 89 |
| 6.25 Multi-Mode Gas Curtain for (a) MM-2 and (b) MM-8 cases. | 89 |
| 6.26 Gas curtain growth (a) and (b), showing the effects of random fluctuations on the post-reshock growth rate. | 90 |

CHAPTER 1

INTRODUCTION AND BACKGROUND

1.1 Introduction

Over the past 100 years, explosives have been used in a wide range of applications. Different types of explosives have different characteristics such as strength, impulse, and heat signatures, that determine the appropriate applications for each. Specific to this study, explosives are being investigated as an effective method to dispose of chemical warfare agents safely and effectively. In order to guarantee the appropriate disposal of chemical agent stockpiles, a deep understanding of the complex physical phenomena that govern explosive blasts is essential. It is practically impossible to gain this understanding from an experimental study because such experiments are dangerous, expensive, and require complex data acquisition methods. For these reasons, the most viable option for gaining an understanding of the physics behind an explosive blast is through computational modeling [1].

Immediately following an explosion, a blast wave propagates outwards, sustained by the high energy source generated by the detonation. Once this blast wave reaches the outer edge of the explosive charge, a shock wave propagates outwards while a rarefaction wave travels inwards. These two phenomena together force an outward acceleration of the detonation products [1]. As the detonation product gases accelerate outward, they can continue to burn with the oxygen in the air and release heat, significantly augmenting the impulse and energy release of the explosive blast [2]. This process is known as afterburning, which is a highly complex phenomena that is governed by hydrodynamic instabilities, mixing, and turbulence [1]. The reaction rate and heat release occurring during the afterburning process are entirely dependent on the mixing of the oxygen in the ambient air with the

outward accelerating detonation products, which relies on a structure caused by instability generation [2]. Therefore, for afterburning to occur at all, there must be mixing between unburned detonation products and air.

Initially, the contact surface separating the detonation products and shocked air is hydrodynamically unstable due to the large density gradient present across it. Therefore, any slight perturbation to this contact surface will result in further growth to this interface's amplitude, creating Rayleigh-Taylor Instabilities [1]. Additionally, as the rarefaction wave propagates inwards it over expands the flow, resulting in a second weak shock travelling outwards that grows in strength due to being accelerated by the detonation products. As this second shock strengthens, it will eventually implode [2]. Travelling inwards, the second shock reflects at the origin and begins to propagate outwards, causing another interaction between the shock and the mixing layer developing, known as reshock. Now with Rayleigh-Taylor instabilities already present, as the secondary shock travels through these instabilities there is baroclinic torque generated due to the misalignment of the pressure and density gradients, resulting in vorticity being imparted to the mixing layer, creating what are commonly known as Richtmyer-Meshkov instabilities (RMI).

A RMI, pictured in Figure 1.1, consists of a domain with two species separated by one contact surface that is impulsively accelerated, which does not accurately represent all of the afterburning interactions occurring during an explosion. Due to the impulsive na-

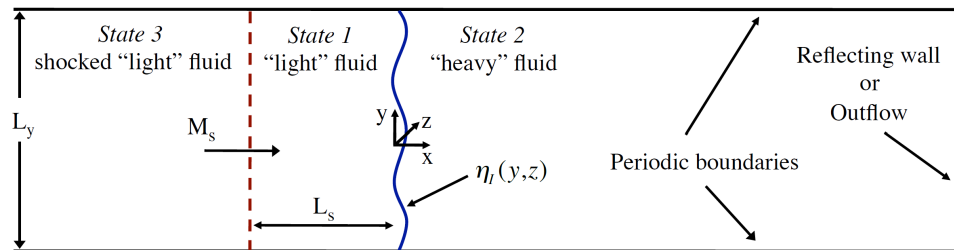


Figure 1.1: RMI Schematic sourced from [3].

ture of the explosion and quick species dispersion, thin layers of detonation products, or “curtains”, develop that have air on either side, creating essentially two contact surfaces

between detonation products and air. Figure 1.2 illustrates the differences between a gas curtain problem and an RMI. The events immediately following an explosion were highlighted solely to expose the significance of the gas curtain mixing problem under reshock, the focus of the current work. Such gas curtains, when impulsively accelerated, produce

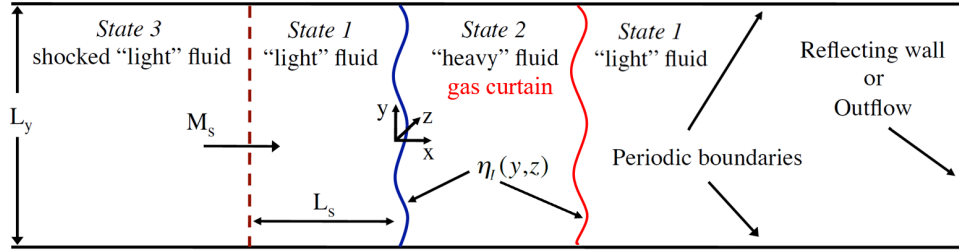


Figure 1.2: Basic Schematic of Gas Curtain.

far more complex flow patterns than RMI configurations [4, 5, 6, 7]. Few studies have been performed on the relationship between the mixing growth of a curtain and its initial shape or thickness [4, 8]. Even fewer studies have investigated a gas curtain's behavior to a reshock [4, 1], where a reshock occurs when a reflected shock passes through the entirety of a developing gas curtain instability. Furthermore, such studies disagree on the connections between a gas curtain's initial conditions and its behavior after reshock. Some studies argue that the post-reshock behavior of a gas curtain is a function of initial conditions, whereas others argue that there is no connection between the two. For these reasons, the objectives of this thesis are to:

1. Investigate the relationship between the gas curtain's initial perturbation shape and the post-reshock mixing layer growth rate.
2. Investigate the relationship between the gas curtain's initial thickness and the post-reshock mixing layer growth rate.
3. Investigate the relationship between the gas curtain's initial perturbation shape and the molecular mixing pre- and post-reshock growth rate.

4. Investigate the relationship between the gas curtain's initial thickness and the molecular mixing pre- and post-reshock growth rate.

These investigations are performed using two-dimensional numerical simulations that utilize the viscous Navier-Stokes equations. Two dimensional simulations will be used for this work because the results of such simulations provide a foundational understanding of the mixing that ensues when a gas curtain is impulsively accelerated, while also maintaining computational efficiency. Three dimensional simulations would be two computationally costly, and previous numerical studies have shown that gas curtain mixing can be understood through two-dimensional studies [9, 5, 4].

CHAPTER 2
LITERATURE REVIEW AND BACKGROUND

2.1 Richtmyer Meshkov Instability

Richtmyer-Meshkov instabilities (RMI) occur when the contact surface between two fluids with different densities is impulsively accelerated, usually by a shock wave [9]. RMIs differ from Rayleigh-Taylor instabilities in that the acceleration of one fluid into the other is impulsive, rather than occurring through a constant force (typically gravity) for Rayleigh-Taylor instabilities. A contact surface is the surface created between two fluids of varying densities, pictured in Figure 2.1. The mixing occurring during an RMI is governed by the inviscid compressible vorticity equation [9]:

$$\frac{D!}{Dt} = \frac{r}{2} \frac{r \rho}{\rho} + ! \cdot r u - !(r \cdot u) \quad (2.1)$$

where ρ is the density, p is the pressure, $! = r \cdot u$ is the vorticity, and u is the velocity. $\frac{D!}{Dt}$ is the material derivative of the vorticity, which is equivalent to $\frac{D}{Dt} = \frac{\partial}{\partial t} + u \cdot \nabla$. The first term on the right-hand side of the vorticity equation is known as the baroclinic torque. As the shock wave travels through the contact surface, baroclinic torque is deposited to the contact surface due to the misalignment of the density and pressure gradients across the interface. This baroclinic torque is a strong driving mechanism of the mixing that occurs during an RMI [9, 10]. This phenomenon can be better understood using Figure 2.1 below [9].

As the shock wave interacts with the interface, the baroclinic torque deposits vorticity to the interface. The vorticity accelerates the interface in a direction consistent with the curl of the density and pressure gradients. After acceleration, the interface's original perturbation

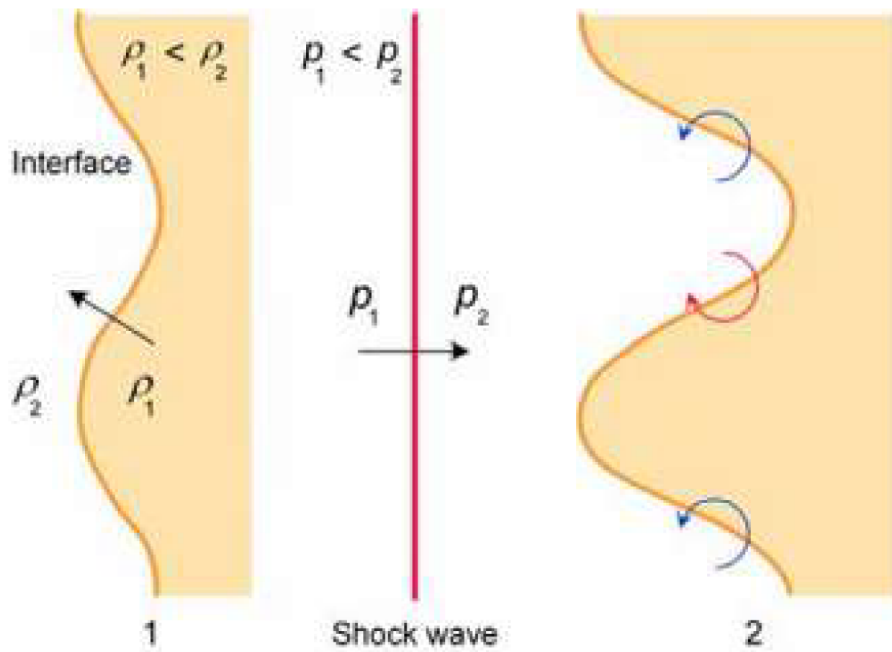


Figure 2.1: Misalignment of Pressure and Density Gradients Over Contact Interface. Sourced from [9].

grows in time, creating what are known as bubbles and spikes, pictured below in Figure 2.2.

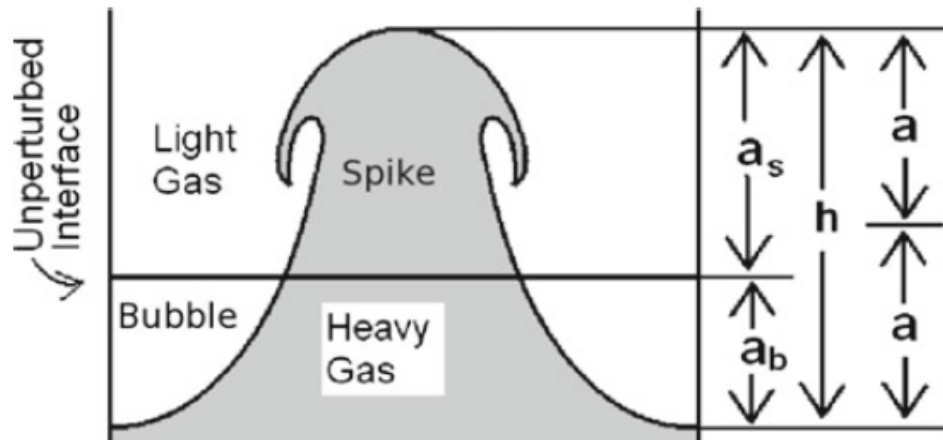


Figure 2.2: Bubble and Spike Definitions, sourced from [9].

A bubble is a region where the lighter fluid penetrates the heavier fluid, whereas a spike is a region where the heavier fluid penetrates the lighter fluid. An RMI can occur in light-heavy and heavy-light configurations, both of which are unstable [9]. A shock that

travels from the light fluid into the heavy fluid (light-heavy configuration) deposits vorticity onto the contact surface that results in growth of the interface's original perturbation [9]. However, a shock that travels through a heavy-light configuration deposits vorticity to the interface that initially reduces the original perturbation, eventually causing the spikes and bubbles to invert and grow in the opposite direction [9]. Spikes and bubbles are known to compete with one another during growth, leading to bubble competition and merger processes that govern the growth of interface perturbations [11]. An initial shock impinging on a curtain resembles a light-heavy and heavy-light configuration superimposed upon one another, with the heavy-light contact surface shifted downstream of the light-heavy interface. This realization may help with the analysis of the results for the curtain problem. However, claiming the results follow that of two superimposed RMI configurations is erroneous because this does not take into account the interaction between the two RMIs, which is clearly present.

2.1.1 Pre-Reshock RMI Growth Rate

In order to have a foundation from which to compare, the mixing that occurs in the curtain problem and in an RMI must be defined. For ease of comparison, the classical mixing definition used in RMI problems will be used. Referring to Figure 2.2, the mixing length is defined as the distance between the tips of the bubble and spike, denoted h . The mean amplitude a is then equivalent to $h/2$. a_s and a_b are simply the distances between the original unperturbed interface and the tips of the spike and bubble respectively. Richtmyer developed a linear growth model of the amplitude $a(t) = a_0 + V_0 t$ based on an impulsive model [12]:

$$a(t) = a_0 + V_0 t \quad (2.2)$$

where a_0 and V_0 are the initial amplitude and Richtmyer velocity respectively. The Richtmyer velocity is defined as:

$$V_0 = k a_0 A V_1 \quad (2.3)$$

where k is the wavenumber, $k = \frac{2\pi}{\lambda}$, λ is the wavelength, and A is the Atwood number defined as:

$$A = \frac{(\rho_2 - \rho_1)}{(\rho_2 + \rho_1)} \quad (2.4)$$

Lastly, ΔV_1 is the change in speed of the interface due to the shock wave, and ρ_1 and ρ_2 represent the densities of the two fluids in the domain. Richtmyer confirmed that the early time growth of a small initial amplitude during an RMI is linear [12]. However, this linear model can only be applied to the early-time growth rate because the later-time growth rate is weakly nonlinear [9]. Furthermore, Holmes *et al.* showed that deviations from linear theory, even in the early time growth stages, occur due to nonlinear and compressibility wave interactions with the interface [13]. In order to overcome this model's limitations, several non-linear potential flow models were developed that were first an extension of a potential flow model for an RTI [9]. Overtime, this extended model became more robust, mainly by extending it further such that the model could be applied to any arbitrary Atwood number [9]. Even with an extensive amount of work done to fine-tune this nonlinear model, the model still failed to accurately match experimental data for late time growth, leading to the development of empirical models. Experimentally, Sadot *et al.* was able to develop an empirical model that combines the initial and asymptotic solution of the potential flow model [14]. Sadot *et al.* constructed a growth rate empirical model of the form [14]:

$$b_{=s}(t) = \frac{1 + \rho_0 k t}{1 + D \rho_0 k t + E \frac{\rho_0^2 k^2 t^2}{\rho_0}} \quad (2.5)$$

where D and E are coefficients that are chosen based on different theoretical models, tabulated in Table 2.1. Because the empirical model of Sadot *et al.* is an empirical curve fit that combines the initial linear growth rate and asymptotic growth, the model is only expected to accurately predict the early and late time growth of an RMI, with discrepancies in the model's results expected between these time periods [3, 14]. This model is also limited to Atwood numbers below 0.9 ($A < 0.9$) and was derived using experimental data for

RMI's occurring with shock speeds below 2.0 ($M_s = 2.0$) [3, 14]. Furthermore, the model assumes potential flow and uses the iso-contour mixing length definition, which leads to further inaccuracies in the model's results [14]. This model will be used to verify the simulation setup later on in this report. Mikaelian was able to obtain an explicit time-dependent model for the nonlinear amplitude growth at late time stages during an RMI that was based on Goncharov's potential flow model for an arbitrary Atwood number [15, 16]. Mikaelian proposed a piece-wise model for the explicit time-dependent amplitude of the perturbation:

$$\begin{aligned}
 \omega(t) = \begin{cases} \omega_0^+ (1 + V_1 k A^+ t) & (t) \leq \frac{1}{3} k \\ \omega_0^+ + \frac{3+A^+}{3(1+A^+)k} \ln[1 + 3 \omega_0^+ k t (\frac{1+A^+}{3+A^+})] & (t) > \frac{1}{3} k \end{cases} \quad (2.6)
 \end{aligned}$$

where A^+ is the post-shock Atwood number and ω_0^+ is the initial post-shock amplitude, estimated by Mikaelian to be:

$$\omega_0^+ = \omega_0 (1 - \frac{V_1}{M_s c_0}) \quad (2.7)$$

where M_s and c_0 are the shock Mach number and speed of sound in the light fluid. Mikaelian's model was developed for two-dimensional RMI growth [17]. Furthermore, Mikaelian's model is only valid in the linear, small amplitude regimes defined by $k \ll 1$ [17]. It is

Table 2.1: Coefficients for Theoretical Models.

| Model | $D_{b=s}$ | $E_{b=s}$ |
|----------------------------|-----------|-----------------------|
| Sadot et al. [14] | $1 - A$ | $3(1 - A) = 2(1 - A)$ |
| Neiderhaus and Jacobs [18] | $1 - A$ | $1 - A$ |
| Goncharov et al. [16] | $1 - A$ | $3(1 - A) = (1 - A)$ |
| Sohn et al. [19] | $1 - A$ | $(2 - A) = 2$ |

important to note that the empirical models above use the iso-contour mixing length definition which neglects the diffusion thickness [9, 20, 3]. This is covered in more detail later. Despite the failures of these models in certain conditions, studying the expressions presented in each model still provides foundational knowledge that reveals the relationships

between the mixing length growth rate and the interface's initial conditions. After analysis of the above expressions, the relationship between the mixing layer growth rate γ_{b-s} and the initial conditions of the RMI can clearly be seen. Specifically, the mixing layer growth rate before reshock depends heavily on the shock strength M_s , the interface's initial amplitude a_0 , wavenumber $k = \frac{2\pi}{\lambda}$, and Atwood number A .

In summary, many theoretical and empirical models for pre-reshock growth rate of a single-mode RMI problem have been validated extensively in literature [21, 14, 9, 12, 17]. Furthermore, a wide number of studies have successfully matched both these models and experimental results through CFD simulations, verifying that the mixing layer growth rate is a direct function of the initial conditions of the RMI [9, 10, 13, 22].

2.1.2 Reshock RMI Growth Rate

Referring to Figure 1.1, a reshock RMI is defined as the mixing that ensues once the developing RMI structure (from first shock passage) is impulsively accelerated a second time by the reflected shock (hence re-shock). Recently, most RMI studies have been focused on the post re-shock growth rate of an RMI due to its greater degree of complexity and relevant applications, such as inertial confinement fusion, scramjet fuel mixing, and supernovae explosions [23]. These numerous applications motivated the development of several analytical models for the post reshock growth rate. Most notably, Mikaelian led this effort by applying the potential flow model he developed for the single-mode RMI to a growing perturbation. [17]. However, all the analytical models developed were functions of the mixing length h_r and wavelength present immediately before reshock, deviating from numerous experimental results that indicated the mixing length growth rate after reshock has no dependence on these parameters [9, 24, 25]. In fact, Leinov *et al.* was the first to show experimentally that the post re-shock growth rate was independent of the mixing length present at reshock, h_r , and that the mixing length growth rate seemed to be only a function of the reshock's strength [25]. Furthermore, Vetter *et al.* showed that the mea-

sured growth rates after reshock were independent of even the interface's initial geometry [24]. Due to the inaccuracies in the simplified analytical models, empirical models were developed. Charakch'an developed an empirical model that was based on two-dimensional RMI numerical studies, expressed as:

$$\frac{dh_2}{dt} = V_2 A \frac{dh_1}{dt} \quad (2.8)$$

where $\frac{dh_1}{dt}$ is the growth rate immediately before reshock, was found to be 1.25 by Charakch'an, and V_2 is the change in speed of the interface due to the second shock [16]. Charakch'an's model is derived by applying a linear empirical fit to numerical results for only two-dimensional single-mode RMIs [16]. Therefore, this model only holds for two-dimensional single-mode RMIs, and it only provides predictions of the initial post-reshock growth rate. Furthermore, Charakch'an developed his empirical expression using numerical analysis with Lagrangian tracking of the interface, resulting in the interface staying sharp throughout the simulation. Using this technique resulted in Charakch'an's model neglecting the effects of the diffusion layer and turbulent mixing, which can be significant factors during an RMI [9]. A second empirical model was developed by Mikaelian, of the form:

$$\frac{dh_2}{dt} = C V_2 A^+ \quad (2.9)$$

where A^+ is the post reshock Atwood number [6]. Mikaelian's model was derived by empirically fitting data for three-dimensional multi-mode RMI numerical results, and as such can only be applied to RMIs of the same configuration [6]. Mikaelian's model closely followed the experimental results of both Vetter and Leinov et al [25, 24], indicating that an appropriate model of the post-reshock growth rate had been developed. Putting this model to the test, Ukai *et al.* [9] numerically investigated the effects of initial conditions on the post reshock growth rate and found that Mikaelian's model can be used to model post reshock growth rates for multi-mode RMI configurations, concluding as well that the

post reshock growth rate does not have any dependence on the initial interface geometry [9]. Furthermore, Ukai *et al.* [9] showed that the post reshock growth rate is linearly proportional to $\sqrt{2}$, which is an indication of the reshock's strength, thus verifying Leinov's original experimental findings [25, 9]. Ukai *et al.* characterized the post-reshock growth rate for an RMI using a "randomness" factor defined as:

$$R = \frac{a_0 k_{max}}{L_y}, \quad (2.10)$$

where a_0 , k_{max} , and L_y are the initial perturbation amplitude, maximum wave number, and length in the transverse direction of the domain, respectively. Ukai *et al.* showed that a higher R leads to lower post-reshock growth rates, showing some dependence of the reshock RMI growth rate on the initial conditions of the interface [9]. Of most importance from the conclusions drawn by Ukai *et al.* however, was that in the case of multi-mode RMI configurations, the post reshock growth rate shows rapid growth if the interface remains sharp at reshock, and slow growth if the interface is mixed at reshock [9]. This result further indicates how Charakch'an's model, Equation 4.3, fails to predict post reshock growth rates because the numerical methods used during development did not allow for the possibility of the interface becoming diffuse and/or mixed before reshock. Expanding upon the effects of interface "sharpness" at reshock, Thornber *et al.* extended Mikaelain's model to include the effect of molecular mixing present immediately before reshock, arguing that a greater presence of molecular mixing before reshock reduces the post-reshock mixing layer growth rate because there is less density variance [26]. Less density variance before reshock indicates that the density gradients across the interface are smaller in magnitude and more random in direction, resulting in a lower magnitude baroclinic torque being generated, thus reducing the post reshock growth rate [26]. The results of Thornber *et al.* [26] provide a robust physical explanation for the findings of Ukai *et al.* [9] and the failures of Charakch'an's model, eliminating ambiguity behind the term mixing layer "sharpness" by

pointing to the direct effect of molecular mixing on the post reshock growth rate. Recently, Bai *et al.* [23] numerically studied the effects of flow non-uniformity on the post reshock growth rate, finding that the mixing layer growth rate after reshock has very little dependence on the degree of non-uniformity in the fluids, proving that the post reshock growth rate is insensitive to yet another initial condition.

In summary, an extensive amount of experimental and numerical studies have been performed that indicate the mixing layer post reshock growth rate is independent of the interface initial geometry, linearly proportional to V_2 , and effected by the presence of molecular mixing before reshock .

2.2 Previous Curtain Studies

A gas curtain is defined as a thin layer of fluid that is surrounded by another fluid on each respective side, pictured in Figure 1.2. Unlike a RMI, a gas curtain has two contact surfaces with density gradients present. The impulsive acceleration of gas curtains occurs in several important applications such as, inertial confinement fusion, supersonic combustion, explosions, and impact dynamics of liquids [7, 1]. Despite the frequency with which curtains of gases experience hydrodynamic instabilities in physical scenarios, there are significantly less studies of gas curtains present when compared with the amount of studies performed on RMIs. Taylor was the first to study finite thickness fluid layers in shock conditions in the context of Rayleigh-Taylor instabilities [27]. Ott studied the non-linear behavior of a gas curtain with a thickness that is very thin compared to its wavelength, developing an analytic solution in two-dimensions, but failing to extrapolate it to three-dimensions. [28]. The first experimental study of shock-accelerated gas curtains was performed by Jenkins et al, who approached the gas curtain problem as two RMI configurations superimposed together [29]. The investigation observed that differences in the initial shapes of the upstream and downstream contact surfaces resulted in three different flow patterns after shock acceleration; (1) independent growth of the two interfaces' initial amplitudes, or vortex pairing

that resulted in either (2) upstream, or (3) downstream mushrooms forming [29]. Limited by the measurement techniques available in 1993, Jenkins *et al.* [29] were unable to interpret the reasoning behind the development of these flow patterns. With no explanations available, Budzinski *et al.* [30] experimentally investigated the same setup through an initial interface shape study, shocking a curtain of SF_6 gas surrounded by air, where it was found that the early-time growth of the gas curtain's two interfaces could be treated as the growth of two independent RMIs, the first being a light-heavy configuration with the latter being a heavy-light configuration. After the early-time growth, during the well-known weakly non-linear regime of a RMI, the growths of each interfaces become highly coupled. Eventually the interface that had a greater initial amplitude dominates, giving rise to the three flow patterns Jenkins *et al.* [29] initially observed. The three flow patterns can be better understood in Figure 2.3. If there are no substantial differences in amplitude magnitudes between the upstream and downstream interfaces, than a sinusoidal flow pattern develops that is consistent with section (a) of Figure 2.3. If the front interface of the gas curtain has the greater initial amplitude, the flow develops into an upstream flow pattern consistent with section (b) of Figure 2.3. If the downstream interface of the gas curtain has the greater initial amplitude, the flow develops into a downstream flow pattern consistent with section (c) of Figure 2.3. The development of the flow pattern can be explained from a vortex dynamics perspective. As discussed earlier, the vorticity generated by the shock interaction with an interface separating two fluids of differing densities is governed by Equation 2.1. The magnitude of the vorticity is greatest where the pressure and density gradients are most misaligned (Figure 2.1). Therefore, the interface with the greater initial amplitude will have the most vorticity deposited to it. As time increases, this causes asymmetrical entrainment of the heavy fluid towards the side with more vorticity. This entrainment eventually results in the mushroom development seen in Figure 2.3 [30].

Baltrusaitis *et al.* [5] numerically investigated the experimental setup of Budzinski *et al.* [30] and Jacobs *et al.* by performing two-dimensional direct numerical simulation using

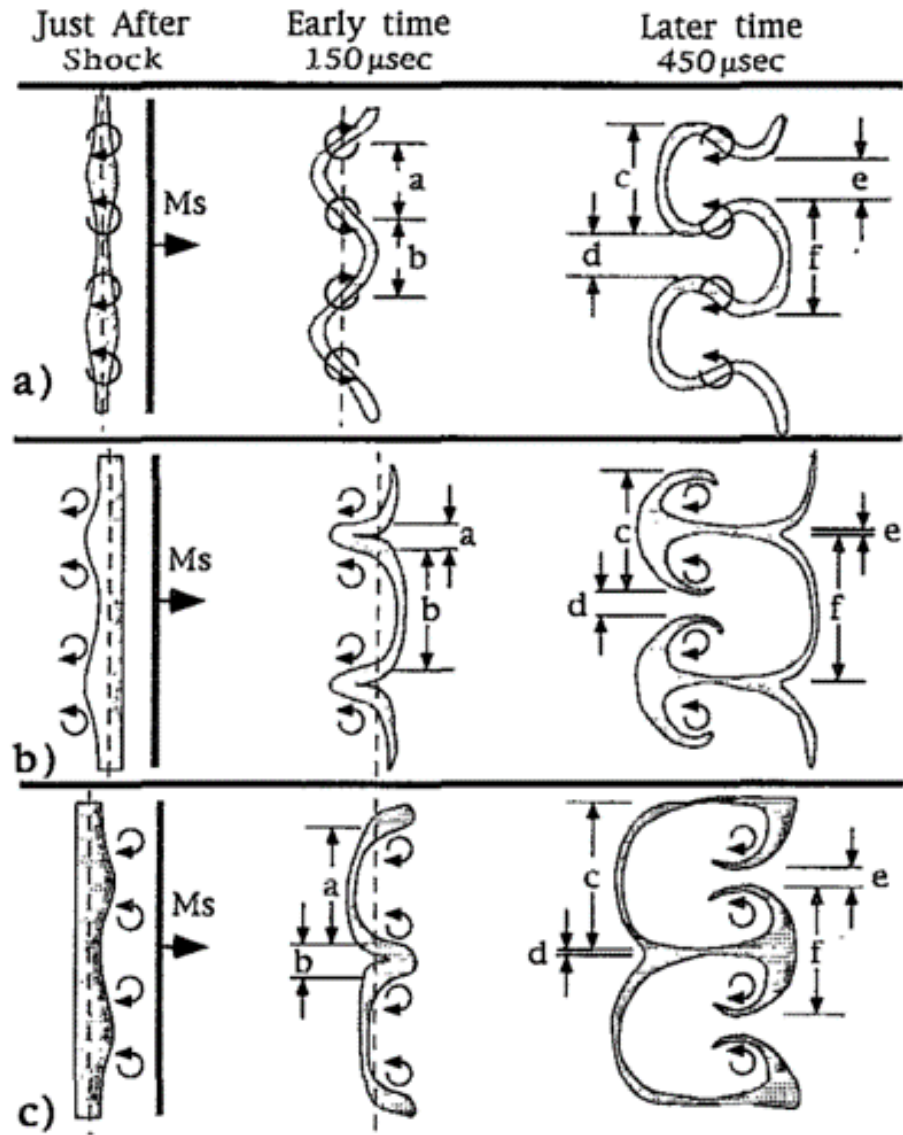


Figure 2.3: Flow Patterns observed during the shock acceleration of a Gas Curtain, sourced from [30].

a Eulerian-based hydrodynamics code that implemented Adaptive Mesh Refinement, producing results that were in agreement with the experimental images of Budzinski *et al.* [30]. The simulation provided new quantitative results, unavailable from experimental studies, that could be used to explain the three emerging flow patterns (i.e. vorticity calculations). Baltrusaitis *et al.* iteratively performed numerical simulations, growing in complexity, until the complexity was sufficient to produce results that matched previous experimental find-

ings [5, 30, 29]. First, Baltrusaitis studied the mixing of pure material curtains (where the curtain is 100% SF_6 surrounded by 100% air, creating a sharp contact discontinuity at the species interfaces), where it was found that the ensuing curtain growth was far greater than the mixing seen in experimental studies [5, 30]. Building in complexity, Baltrusaitis *et al.* then numerically simulated the mixing of an initially mixed curtain where the curtain had diffuse interfaces, representing a more physically realistic scenario. As expected, the ensuing growth for this case was less than that for the pure curtain, because the diffuse interfaces resulted in less vorticity generation due to a smaller-in-magnitude density gradient across the interfaces [5]. Lastly, Baltrusaitis *et al.* [5] simulated the initial curtain conditions provided by the experimental study of Budzinski *et al.*, producing results that matched the experimental results of [30] very closely. Despite the close match, Baltrusaitis *et al.* highlighted the discrepancies between the numerical results and available experimental results, suggesting that such discrepancies can be attributed to the limitations of two-dimensional analysis [5]. It is well-known that three-dimensional flow features (that do not exist in two-dimensions), such as vortex stretching, have a strong influence on fluid mixing. This influence is inherently neglected in two-dimensional simulations. Through this iterative investigation, Baltrusaitis *et al.* [5] found that the growth of the perturbations of the gas curtain in both the linear and nonlinear regime before reshock were extremely sensitive to the initial conditions, mainly the initial mass distribution. This finding is analogous with the behavior of a RMI, where the pre- and post-reshock growth rate is highly dependent on the "sharpness" of the initial interface. This result is also corroborated by several other studies that emphasize more complex initial perturbations in the interfaces lead to enhanced vortex interactions and mixing [4, 5, 6, 7]. A more diffuse initial curtain diminishes the strength of the density gradients, that when impulsively accelerated by a shock wave, leads to a smaller amount of vorticity being deposited to the curtain's interfaces because less baroclinic torque is generated. Baltrusaitis *et al.* [5] emphasized that small differences in the initial conditions can yield drastically different mixing dynamics

because the interactions between the curtain’s interfaces act to amplify these differences, illustrating that small changes in initial conditions for a gas curtain have a far more significant impact on dynamic behavior than they do for single-interface RMI scenarios [30]. In concluding remarks, Baltrusaitis *et al.* [5] made note that the flow patterns arising from a shock-accelerated gas curtain were far more complex than the single-interface interactions seen in RMIs, because of the interactions between the two growing interfaces and an increased amount of wave reverberations present in the curtain. Shock interactions with the gas curtain occur far after shock passage in the form of multiple reflections and refractions of the initial shock [5, 8, 31, 4].

Balasubramanian *et al.* performed an experimental investigation of gas curtain instabilities’ dependence on initial conditions by shocking varicose SF_6 gas curtains and taking PLIF and PIV diagnostic images [31]. Most notably Balasubramanian *et al.* characterized the initial shape of each tested gas curtain by the root-mean-squared slope of the interface, defined to be:

$$k_0 = \frac{2}{\lambda_0} a_0 \quad (2.11)$$

where λ_0 and a_0 are the curtain’s interfacial initial wavelength and amplitude respectively. Adopted from the study of single-interface RMIs, the rms slope of the interface was applied to the study of gas curtain instabilities by [31] because it is directly proportional to the amount of vorticity generated (on an interface) by the passage of the shock wave [31]. Testing short and long wavelength curtains (large and small λ_0 ’s), and a multi-modal curtain, Balasubramanian *et al.* showed that Equation 2.11 could be use to qualitatively predict the mixing growth rate that ensues after shock passage. The larger the wavelength (smaller λ_0), the greater the curtain growth rate because there is less vorticity competition and transverse motion generated (and vice versa) [31, 9]. Contradictory to single-interface RMI behavior [9], Balasubramanian *et al.* [31] found that the multi-modal curtain exhibited a greater curtain growth rate than its single-mode counter parts. This is an interesting claim that will be tested later by the current work. From a molecular mixing perspective how-

ever, Balasubramanian *et al.* argued that a more complex initial curtain geometry leads to a more well-mixed state [31, 32], consistent with single-interface RMI behavior. Through the initial condition investigation, Balasubramanian *et al.* [31] concluded that modal merging and competition are extremely important phenomena that greatly influence the mixing dynamics of gas curtain instabilities. It is interesting to note that Balasubramanian's characterization of gas curtains does not account for changes to curtain thickness.

Following these experiments, analytical growth models were developed. Mikaelian developed an analytical linear growth model for the growth of perturbations on the surface of a curtain, that assumed incompressibility and that the initial perturbations were small and linear ($\delta_i(0)k \ll 1$), taking the form [17]:

$$\delta_1(\tau) = \delta_1(0) \left(\frac{v}{\cos(\theta)} \right)^2 [\delta_1(0) \sin(\theta) \delta_2(0)] \quad (2.12)$$

$$\delta_2(\tau) = \delta_2(0) \left(\frac{v}{\cos(\theta)} \right)^2 [\delta_2(0) \sin(\theta) \delta_1(0)] \quad (2.13)$$

where δ_1 and δ_2 are the shape functions for the upstream and downstream curtain interfaces, respectively, v is the jump velocity imparted to the interfaces, τ is time, and θ is the coupling angle between the two interfaces defined by:

$$\sin(\theta) = (2W_1 = W_2) = [1 + (W_1 = W_2)^2] \quad (2.14)$$

where W_1 and W_2 are the upstream and downstream perturbed interface velocities after shock acceleration, respectively [17]:

$$\frac{W_1}{W_2} = 1 + ST + \frac{S}{R} \left(1 + \frac{P}{1 + R^2 + 2R \coth(kt)} \right); \quad (2.15)$$

where, $R = \frac{2}{1}$, $S = \sinh(kt)$, $T = \tanh(kt=2)$, and:

$$^2 = \rho \frac{k_0(R - 1)}{1 + R^2 + 2R \coth(kt)}; \quad (2.16)$$

where $k_0 = \frac{2}{0}$, and t is the thickness of the curtain. This model will be tested for the single-mode curtain simulations performed in the current work. Mikaelian's model neglected all non-linear effects, assumed sharp interfaces, and did not consider the presence of wave reverberations within the curtain, therefore only providing theoretical insight to the gas curtain instability [17]. Even in this limited linear model, the perturbation growths of each interface after shock acceleration were shown to be highly coupled. Mikaelian pointed out that in the scenario where either interface had zero initial perturbations, the zero-perturbation interface would still experience perturbation growth because of the feed-through from the other interface [17]. Mikaelian later tested his analytical model with two-dimensional direct numerical simulations using an arbitrary Lagrangian/Eulerian hydrocode, verifying that the analytical model predicted flow patterns well, despite the incompressible assumption. [33]. His numerical results also matched the experimental results available at the time with good agreement [30, 29, 7]. Testing several different initial interface shapes using the developed analytical model, Mikaelian [33] showed that if $\rho_1 = \rho_2$, which creates an initial sinuous gas curtain with uniform thickness, Equation 2.12 predicts that the normalized growth rates ($NGR_i = \frac{i}{0} vk$) of the upstream (1) and downstream (2) interfaces will be equal in magnitude but opposite in sign. Considering the limit where $kt \gg 1$, which represents a thick gas curtain, Mikaelian's model predicts that the gas curtain instability reduces into two independent RMI growths [33]. When the interfaces are too far apart to communicate, their respective perturbations are able to grow independently, leading to an increase in curtain width growth [33]. Another important claim of Mikaelian's [33] work is in the opposite limit, when $kt \ll 1$, representing a very thin curtain. In this scenario, Mikaelian's model predicts that the interfaces would share the

same growth rate for all time, due to their proximity to one another [33]. This case represents an extreme form of interface coupling, a behavior that is exclusive to gas curtain instabilities. Furthermore, Mikaelian predicted that a fourth flow pattern would emerge, consisting of opposite mushroom development, if the nozzle used during experiments was switched from varicose-shaped to sinuous-shaped [33]. In concluding remarks, Mikaelian highlighted the difficulty of the gas curtain problem, stating that "the compressible problem of finite-thickness layer must be dauntingly difficult since it involves both types of interfaces (light-heavy and heavy-light) with perturbed shocks and rarefactions going back and forth between them" [33]. It is important to remember, however, that Mikaelian's simple model, Equation 2.12, neglects non-linearity, compressibility, and the presence of density gradients in a gas curtain, making it an accurate qualitative predictor of only very early time growth of the gas curtain after shockage.

A few other analytical models were developed for gas curtain growth, such as Jacobs *et al.* [34] who derived a point vortex model for the nonlinear growth at later times of a gas curtain instability that assumes uniformly spaced counter-rotating vortices. With numerical studies [33] matching the limited experimental results [34, 30] for gas curtains of the time, the study of gas curtains begged for more experimental studies to be performed. Performing experimental gas curtain studies proved to be extremely difficult, however, because curtain generation capabilities were extremely limited, resulting in the production of unstable gas curtains that make drawing any conclusive findings inherently erroneous [8]. Balakumar *et al.* [8] overcame this experimental limitation by using a newly developed passive co-flow configured nozzle, which proved to be significantly more stable than past nozzle configurations [8]. Using this nozzle, Balakumar *et al.* [8] obtained experimental results that matched the point vortex model of Jacobs *et al.* [29], by accelerating a curtain of SF_6 with a $M = 1.2$ shock wave, while taking simultaneous particle-image velocimetry and planar laser-induced fluorescence measurements of the gas curtain during the experiment. This experiment showed that the early time growth resembles the growth of two

independent RMIs, supporting the early findings of Jenkins *et al.* [29] and Budzinski *et al.* [30] through updated experimental methods. The upstream interface amplitude grows while the downstream interface inverts in phase and then begins to grow in amplitude, consistent with the growth of light-heavy and heavy-light RMI configurations, respectively. Thanks to the updated experimental methods of Balakumar *et al.* [8] however, the measurements indicated the presence of slight asymmetries in the developed flow patterns due to the small differences in shock strengths between the interface accelerations, the time for phase inversion of the downstream interface, and the enhanced vorticity deposit on the downstream interface resulting from the deformation of the shock after passage through the upstream interface. Furthermore, Balakumar *et al.* [8] performed the first experimental re-shock gas curtain experiment, which will be discussed in detail in the next section of this work. Two numerical investigations [4, 7] managed to match the experimental results of Balakumar *et al.* [8]. Shankar and Lele [7] highlighted the vortex pairing structure that occurs on each of the curtain's interfaces after shock passage. Referring to Figure 2.3 and Figure 2.1, the sinusoidal shape of each interface results in initial vorticity deposition that is equal in magnitude (if no random fluctuations are present) and opposite in sign, creating "vortex pairs" that lead to the asymmetrical entrainment and mushroom development discussed previously. After matching the experimental results of [31] and [8], Gowardhan *et al.* [4] extrapolated [31]'s rms slope characterization to be more directly applicable to curtain instabilities, by defining a curtain's rms slope as:

$$\sigma_0 = k_0 w_0 = \frac{2}{\lambda_0} w_0 \quad (2.17)$$

where in Gowardhan's definition w_0 denotes the curtain's initial thickness. Notice that Gowardhan's characterization does not consider amplitude of the curtain's perturbations. Using this characterization, Gowardhan *et al.* tested several different curtain shapes, showing that curtains characterized by high σ_0 's result in lower gas curtain growth in time after

initial shock passage, due to modal competition and increased transverse motion. This result is consistent with [31]’s findings, and the behavior of single-interface RMIs [9, 3, 32].

2.3 Previous Reshock Curtain Studies

In the current work, a reshock curtain problem is defined as the event when the developing mixing, caused by the initial shock passage through a gas curtain, is impulsively shocked a second time by the reflected shock that reflected off of the far wall of the channel (see Figure 1.2). Balakumar *et al.* [8] continued the study of gas curtain instabilities by obtaining the first experimental results of a reshock event occurring on a gas curtain instability, by placing a reflecting wall at the end of the shock-tube. Therefore, reshock of a gas curtain is defined as the event when a reflected shock wave passes through the gas curtain instability. From this experiment, Balakumar *et al.* [8] showed that the reshock event causes a ”dramatic” increase in mixing and significant amplification of the curtain growth rate. This behavior is consistent with single-interface reshock RMI behavior [9, 26, 25, 23]. Because the reflected shock wave passes through an already developed curtain instability (with vorticity and mixing present), the shock deposits greater vorticity over a wider range of scales for a given density gradient [9, 8]. The additional energy supplied to the evolving structure by the reflected shock wave causes the amplified growth rate and mixing [8]. Through qualitative examination of the PIV-PLIF images, Balakumar *et al.* claimed that the reshock event dramatically redistributed the vorticity scales, producing a plethora of small vortices at the expense of the large-scale structures. This redistribution of vorticity to smaller scales is credited as the cause of the rapid mixing after reshock. Balakumar *et al.* [8] came to the conclusion that the curtain loses memory of its initial conditions after reshock due to this drastic change in scales.

Mikaelian’s [33] numerical results for a reshock of a gas curtain led to the same conclusion. Testing several different initial perturbation configurations, Mikaelian showed that

despite each configuration leading to different mixing lengths immediately before reshock, after reshock the mixing lengths and mixing layer growth rates were essentially the same for all cases [33]. A second impulsive acceleration of a gas curtain increases mixing dramatically and amplifies the growth rate of the instabilities. According to Mikaelian [33] and Balakumar *et al.* [8], the growth rate amplification upon reshock is dependent on only the reshock strength, the curvature of the evolving structure, and the magnitude of the density gradients present, indicating independence of the post reshock growth rate from the curtain's initial geometry [6, 8]. Again, this is consistent with the behaviors of a reshock RMI configuration, where the magnitude of the density gradients and curvature of the evolving structure at reshock are more familiarly defined as the degree of "sharpness" of the interfaces undergoing reshock.

After matching the experimental results of Balakumar *et al.* [8] numerically, Shankar and Lele [7], and Gowardhan *et al.* [4] launched their own numerical investigations of reshock gas curtain instabilities. Shankar and Lele [7] agreed that the vorticity deposited at reshock destroys the ordered velocity field present in the flow and deposits higher energy into the non-linear flow, causing break up of the large scale structures into a more chaotic flow field. However, in addition to matching both the results of Balakumar *et al.* [8] and Shankar and Lele [7], Gowardhan *et al.* [4] performed a numerical analysis on the sensitivity of the gas curtain's post reshock mixing length to the initial conditions. Isolating only the initial interface rms slope, θ_0 (defined in Equation 2.17), the study concluded that the mixing length post reshock was in fact dependent on θ_0 , an initial geometrical condition. The addition of random fluctuations into θ_0 (increasing the complexity of curtain initial conditions) led to an increase in vortex interactions and thus mixing after reshock [4]. Essentially, Gowardhan *et al.* argues that the inclusion of random fluctuations in the curtain's initial conditions, which is known to lead to enhanced re-distribution of the large scale vortices into small scales upon reshock, actually increases the curtain growth rate after reshock. This behavior is contradicting to single-interface RMI behavior, where

an increase in the randomness of the single-interface initial shape leads to a decrease in curtain growth post reshock [9, 26]. Balasubramanian *et al.* [31] experimentally came to the same conclusion by performing a parametric study of the effect of the curtain's initial amplitude and wave number on post reshock mixing, claiming that the mixing at late times was dependent on the initial conditions isolated in the study. Given these findings, there is a clear contradiction in literature on the dependence of a gas curtain's post-reshock growth rate on the initial conditions that begs for further research to be performed.

In summary, a limited amount of studies have been performed that indicate the growth rate of perturbations in a gas curtain upon shock-acceleration are highly dependent on the initial conditions of the curtain before reshock. After reshock however, literature strongly debates on whether there is or is not memory of initial conditions present in the mixing growth. It is clear, however, that the reflected shock provides additional energy to the instability that cascades the large scale vorticity into smaller scales, enhancing the post reshock mixing [4, 8, 7, 31]. Whether or not the enhancement of mixing post reshock, mainly the post reshock curtain growth rate, is connected to changes in the curtain's initial shape (which would allow some level of flow control) remains to be unanswered. Furthermore, previous studies focused almost entirely on the effects of differing initial conditions between the upstream and downstream interfaces of a gas curtain, while no studies isolated the effects of initial gas curtain thickness on the ensuing mixing layer growth.

CHAPTER 3

OBJECTIVES

The primary objective of this thesis is to study the gas curtain's behavior under reshock. Specifically, the current work intends to investigate both the molecular mixing and structure width growth that occurs following the shock acceleration of a gas curtain. The shock-acceleration of a gas curtain occurs in several important physical scenarios [7, 1]. Past studies concerning gas curtains seem to only focus on the effect of differing initial conditions between the upstream and downstream interfaces of the curtain, with a minimal amount of studies even investigating the response of a gas curtain to a reshock [8, 4, 33]. Furthermore, the few conclusions drawn in literature about a gas curtain's response to reshock disagree about the relationship between the gas curtain's initial conditions and post reshock mixing layer growth rate. Some studies [6, 8] claim that the gas curtain's post reshock mixing layer growth rate is not a function of its initial conditions, whereas other studies [4] claim that it is. Given these observations, it is clear that there is still a high degree of uncertainty in the post reshock growth rate of gas curtain perturbations, most likely due to the complexity of the problem resulting from the high degree of coupling between the interfaces and presence of many wave reverberations within the gas curtain [5]. Furthermore, no studies have investigated the relationship between the gas curtain's thickness and the post reshock mixing layer growth rate. It is clear that as the thickness of the gas curtain grows, the solution asymptotes towards the RMI solution, because the initial domain returns to that of an RMI. Revealing this transition between solutions will provide deeper physical understanding of the gas curtain problem and how it differs from a RMI. Additionally, because molecular mixing is difficult to quantify experimentally, past studies have mainly focused solely on structure width calculations for gas curtain instabilities [25, 8]. Following suit, numerical investigations of gas curtains also focused on the structure width of a gas curtain instabil-

ity because only this parameter could be verified from previous experimental studies [4, 5, 33]. In order to provide new insight, the current thesis intends to investigate the molecular mixing that occurs during shock acceleration of a gas curtain as well as the post reshock mixing layer growth rate of the gas curtain.

The objectives of the thesis are properly defined in the following paragraph. The current thesis intends to investigate the connection between the gas curtain's post reshock mixing layer growth rate and its initial conditions through the following objectives:

1. Investigate the relationship between the gas curtain's initial perturbation shape and the post-reshock mixing layer growth rate.
2. Investigate the relationship between the gas curtain's initial thickness and the post-reshock mixing layer growth rate.

Additionally, the current work intends to investigate the effects of the gas curtain's initial conditions on the molecular mixing that occurs post initial shock and reshock passage, through the following objectives:

3. Investigate the relationship between the gas curtain's initial perturbation shape and the molecular mixing pre- and post-reshock growth rate.
4. Investigate the relationship between the gas curtain's initial thickness and the molecular mixing pre- and post-reshock growth rate.

These investigations will be performed on single-mode and multi-mode in-phase gas curtain configurations. Gaining this understanding will give insight into the afterburning process of an explosion, which includes interactions between detonation products and air [1]. Each study will be performed through two-dimensional numerical investigations that are based upon the unsteady, compressible Navier-Stokes equations. It is important to note that, unlike previous studies, the parametric investigations will be performed with the upstream and downstream perturbations kept equivalent and in-phase, $\phi_1(0) = \phi_2(0)$. Apply-

ing this equivalence isolates the effects of the initial conditions being studied in this work on the mixing layer growth rate and molecular mixing occurring [29, 8, 30, 33].

Before these objectives can be met, verification of the numerical simulation will be performed by matching results of a previous numerical RMI study, and matching both experimental and numerical results for gas curtain instabilities [9, 8, 5]. This verification process is discussed in detail in the following chapter.

CHAPTER 4

SIMULATION METHODOLOGY AND SET-UP

4.1 Simulation Methodology

The simulations are conducted using the Navier-Stokes equations in an unsteady and compressible form as:

$$\frac{\partial \rho}{\partial t} + \frac{\partial (\rho u_i)}{\partial x_i} = 0 \quad (4.1)$$

$$\frac{\partial (\rho u_i)}{\partial t} + \frac{\partial}{\partial x_i} [\rho u_i u_j + P \delta_{ij} - \tau_{ij}] = 0 \quad (4.2)$$

$$\frac{\partial E}{\partial t} + \frac{\partial}{\partial x_i} [(E + P)u_i + q_i - u_j \tau_{ij}] = 0 \quad (4.3)$$

$$\frac{\partial Y_k}{\partial t} + \frac{\partial}{\partial x_i} [(Y_k u_i + J_{i;k})] = 0; k = 1; \dots; N_s; \quad (4.4)$$

for the continuity, momentum, energy, and species equations, respectively. In the above equations, ρ is the density, u_i is the velocity vector in cartesian coordinates, P is the pressure, τ_{ij} is the component of the shear stress tensor acting on the surface of the fluid element normal to direction i acting in the j direction. E is the total energy, Y_k is the species mass-fraction for species k , q_i is the rate of heat transfer, and N_s is the total number of species in the flow. Each of these parameters can be further defined using fundamental thermodynamics. The total energy is:

$$E = e + \frac{1}{2} u_k u_k; \quad (4.5)$$

where e is the internal energy, defined as:

$$e = \sum_{k=1}^{\mathcal{N}_s} Y_k h_k \quad \frac{P}{\rho}; \quad (4.6)$$

where h_k is the sensible enthalpy of species k , which is defined as:

$$h_k(T) = h_{f,k}^0 + C_{P,k}[T - T_0] \quad (4.7)$$

where T is the current temperature and T_0 is the reference temperature. Additionally, $h_{f,k}^0$ is the enthalpy of formation at the reference pressure and temperature for species k , and $C_{P,k}$ is the specific heat at constant pressure for species k . The equation above for each species' sensible enthalpy results from making the calorically perfect gas assumption. Simulations were performed assuming all species are calorically perfect gases. At the temperatures considered in this study, this is a reasonable assumption, especially considering that no reactions are allowed to occur because only mixing is being studied. Furthermore, the calorically perfect gas assumption is a common assumption of past RMI studies [9, 26, 17]. Using the perfect gas assumption, the equation of state becomes the well-known perfect gas law, expressed as:

$$P = \rho R T; \quad (4.8)$$

where R is the specific gas constant:

$$R = \sum_{k=1}^{\mathcal{N}_s} Y_k \frac{R_u}{MW_k} \quad (4.9)$$

where R_u is the universal gas constant, defined to be $8,314.51 \frac{J}{kmolK}$. Additionally, MW_k is the molecular weight of species k .

Referring to the Navier-Stokes equations presented previously, the transport properties in these equations must be properly defined. In order to accomplish this, it was assumed

that the simulated fluids were Newtonian in nature, meaning that their shear stress tensors are proportional to their rate of strains, a common assumption [17, 9, 23]:

$$\tau_{ij} = \left(\frac{\partial U_i}{\partial X_j} + \frac{\partial U_j}{\partial X_i} \right) \frac{2}{3} \mu_{ij} \frac{\partial U_k}{\partial X_k}; \quad (4.10)$$

where μ_{ij} is the molecular viscosity coefficient, given by Wilke's formula [9].

$$\mu_{ij} = \frac{\mu_s}{\sum_{k=1}^{N_s} X_k} \frac{\mu_k}{X_k}; \quad (4.11)$$

where μ_k is the k -th species viscosity, and:

$$\mu_k = \left[1 + \left(\frac{\mu_j}{\mu_k} \right)^{\frac{1}{2}} \left(\frac{MW_j}{MW_k} \right)^{\frac{1}{4}} \right]^2; \quad (4.12)$$

if $i < j$, otherwise if $i = j$, $\mu_{ij} = \mu_k$. Assuming the heat conduction rate is proportional to the local temperature gradient, Fourier's Law was used to compute the rate of heat transfer. Additionally, due to the high level of mixing in an RMI problem, the enthalpy changes due to species diffusion must be included in calculations as well [9]. Therefore, the total heat flux is given as:

$$q_i = -\frac{\partial T}{\partial X_i} + \sum_{k=1}^{N_s} Y_k h_k V_{i;k}; \quad (4.13)$$

where κ and $V_{i;k}$ are the thermal conductivity and diffusion velocities. In this study, the diffusion velocities were calculated using the mixture average formulation, defined as:

$$V_{i;k} = \frac{1}{X_k} D_{km} \frac{\partial X_k}{\partial X_i}; \quad (4.14)$$

where X_k is the mole fraction of species k , and D_{km} is the mixture diffusion coefficient of species k . The mixture diffusion coefficient of the species k is defined to be:

$$D_{km} = \frac{\sum_{j \neq k}^{N_s} X_j MW_j}{MW_m} \frac{1}{\sum_{j \neq k}^{N_s} X_j} = D_{jk}; \quad (4.15)$$

Where D_{jk} is the binary diffusion coefficient between species i and j , which is a function of temperature, computed using a curve fit. Because the diffusion velocity does not satisfy mass conservation ($\sum_{k=1}^{N_s} V_{ik} Y_k \neq 0$), the correction velocity must be used to adjust the mass flow:

$$V_i^C = \sum_{k=1}^{N_s} Y_k \left(\frac{1}{X_k} D_{km} \frac{\partial X_k}{\partial X_i} \right); \quad (4.16)$$

Resulting in the species diffusion flux $J_{i;k}$ being computed as:

$$J_{i;k} = Y_k (V_{i;k} + V_i^C); \quad (4.17)$$

The thermal conductivity is calculated according to:

$$= \frac{1}{2} \left(\sum_{k=1}^{N_s} X_k \kappa_k + \frac{1}{\sum_{k=1}^{N_s} X_k} \right) \quad (4.18)$$

where κ_k is the pure species conductivity of the k -th species, computed using a curve fit.

With the transport properties fully defined, the Navier-Stokes equations can be solved.

4.2 Numerical Formulation

Due to the nature of the simulation, a numerical solver must be used that can account for the effects of both shocks and hydrodynamic instabilities. The mixing growth in the simulation leads to large gradients in the fluid and smooth regions, both of which must be captured. In this study, this is accomplished by using a higher-order scheme that resolves smooth regions and regions of discontinuity simultaneously. The numerical solver uses a second-order central scheme that has been adapted to turbulent simulations in smooth regions. In regions of large gradients, the flux evaluation reverts to a third-order flux difference splitting method. At discontinuities, the Monotone Upstream-centered Schemes for Conservation Laws (MUSCL) approach reconstructs the flux, and a hybrid Riemann solver (HLLC/E) is applied to compute fluxes. This hybrid scheme has been proven to be robust

by numerous studies [9, 3, 35]. The simulation methodology and numerical formulation are the chosen inputs for the computational fluid dynamics code used in this work, known as LESLIE. LESLIE is a finite-volume/finite-difference, compressible flow solver for multi-physics simulations developed at the Georgia Tech Computational Combustion Laboratory. The next sections describe each component of the numerical formulation briefly.

4.2.1 Finite Volume Method

The central scheme used during simulation is a finite volume method that expresses the governing equations in conservative form, allowing the Navier-Stokes equations to be solved by applying conservation principles to a control volume. This allows the changes in mass, momentum, energy, and species composition within the control volume to be determined by the net flux of each respective quantity and source term. Using a structured grid, the control volume consists of six surface elements (f) forming a three-dimensional computation. A cell-centered scheme is employed that stores the state variable values at the center of each cell. Because the cells are square and uniformly spaced at all time, a curvilinear physical domain (x, y, z) can be transformed into the uniform computational domain (ξ, η, ζ) . Performing this transformation on the conservative form of the governing equations is a form of MacCormack's method, which computes the fluxes at the cell faces by alternating upwind- and downwind-biased differencing, the sum of which gives a higher order central flux computation. This process results in second-order accuracy in space when used with MacCormack's time integration scheme, described below [9].

4.2.2 Time Integration - MacCormack Scheme

MacCormack's time integration method is a finite-volume method that couples the time and spatial integration schemes. This is accomplished using an explicit predictor-corrector scheme, where the predictor step is computed based on the current time step's state variable values, and correcting step is calculated using the predictor step values. The time step Δt

is determined by the properties in the cell at each step in time. If there are high velocities present in the cell, the Δt is decreased to ensure accuracy. In order to compute the viscous fluxes, face-averaged derivatives are computed using a finite difference-*like* approach, where the partial derivatives representing the transformation between the curvilinear coordinates to the uniform computational domain are determined from the grid and stored during simulation start-up. Using this methodology, the derivative for any cell averaged variable is computed using a second-order central explicit method.

4.2.3 Central Schemes

In smooth regions a central scheme is used to compute fluxes because it is minimally dissipative. Using the state variables at the cell interface, the flux at the cell interface is computed using forward and backward differencing. The differencing direction is chosen based on the predictor and corrector steps defined earlier, maintaining the order of the scheme. Furthermore, switching the differencing direction at each iteration ensures that the solution is not biased by direction [9].

4.2.4 Flux Difference Splitting Method

In order to avoid numerical oscillations caused by central schemes when resolving discontinuities, upwinding schemes are applied near discontinuities. The flux difference splitting method computes the flux based on the wave propagation. Monotone Upstream Centered Scheme for Conservation Laws (MUSCL) is used to maintain the high-order of the solutions, and the flux is computed by a hybrid HLLC/E Riemann solver scheme. This flux difference splitting method only applies to the inviscid flux computations, with the viscous flux computations detailed previously. The HLLC/E scheme switches between HLLC and HLLC/E schemes depending on flow conditions [9, 16]. The basis of any HLL (Hartan, Lax and Leer) Riemann solver is the assumption that there are two waves within the computational cell moving in opposite directions, creating three regions of differing solutions

within the cell domain [36]. The scheme becomes an HLLE scheme when the wave speed (or characteristic velocity U) is determined using Einfeldt's scheme [37, 38]. The HLLC method adds a contact surface to the original HLL method [39, 9]. Combining these two Riemann solvers capitalizes on the low diffusiveness of the HLLC scheme, while avoiding the carbuncle effect induced by the HLLC scheme through switching to the HLLE scheme [9]. The switch between the two schemes is based on whether a shock (sharp discontinuity) is detected within a computational cell. If a shock is detected, the HLLE scheme is used transverse to the shock front while in the shock region [9, 39]. In order to maintain the high-order solution, the hybrid finite-volume formulation is used to integrate the conservation equations. The numerical scheme incorporates a fourth-order central scheme in smooth regions, while (for flux evaluation) reverting to a high-order flux difference splitting method in regions of strong gradients (shocks). The foundational equations for these schemes are excluded from this work for brevity. The reader is referred to [20] for a detailed review of this numerical formulation. Additionally, more information on specific components of the formulation can be found in: [9, 16, 19, 35, 40, 41, 36, 37, 38, 42, 39].

4.3 Mixing Quantification

4.3.1 Mixing Length

Upon vorticity deposition to an interface, the interface's amplitude initially grows linearly. Once the two fluids become entrained and begin to mix, the mixing layer growth rate saturates and becomes nonlinear [3]. In practice there are many mixing length definitions used. Most commonly, the mixing length is defined using the integral definition:

$$\lambda(t) = \int_{x=0}^{x=L_x} \overline{hY_{mix}} dx = 4 \int_{x=0}^{x=L_x} \overline{hY_h} / (1 - \overline{hY_h}) dx: \quad (4.19)$$

where the quantity \overline{h} represents a planar average in two-dimensions in the transverse direction and is a function of only the time, t , and x , the longitudinal direction. The factor of

4 in Equation 4.19 results from the substitution of the mixed mass fraction definition Y_{mix} [43, 44]:

$$Y_{mix} = \begin{cases} 2Y_h & \text{if } Y_h \leq \frac{1}{2}; \\ 2(1 - Y_h) & \text{if } Y_h > \frac{1}{2}; \end{cases} \quad (4.20)$$

where hY_h is the mass fraction of the heavy fluid, SF_6 in the current work. Notice that if hY_h is 0.5 at some stream-wise location, the integrand of Equation 4.19 becomes $\frac{1}{4}$. The factor of 4 allows the integrand to become normalized to unity when $hY_h = 0.5$. Additionally, if hY_h is 0 or unity, the integrand becomes zero, indicating a location in the stream-wise direction where there is no mixing present.

Another mixing length definition commonly used is known as the threshold method, defined as the region where $\epsilon < hY_{SF_6} < 1 - \epsilon$. ϵ is a manually set tolerance level, defined to be $\epsilon = 0.01$ in this study [20, 9, 3]. The threshold method was used by Ukai *et al.* [9], who's data is used for verification of mixing length calculations later in this work.

Recall that several empirical models were developed that calculate the iso-contour mixing length. The empirical model from Sadot *et al.* is displayed in Equation 2.5 and tables of coefficients for the varying models are tabulated in Table 2.1. The iso-contour mixing length is a measure of the iso-contour of the mass fraction, pictured in Figure 4.1, resulting in a neglect of the diffusion thickness. Each iso-contour mixing length produced by the models found in Table 2.1 are plotted in Figure 5.2 and used for verification of the mixing length calculation used in this work.

4.3.2 Gas Curtain Width Calculation

Extrapolating the concept of mixing length to gas curtain instabilities, the gas curtain width can be defined using different methods. Based on the integral definition of the mixing length, past studies have defined the gas curtain width as the shock-wise distance over

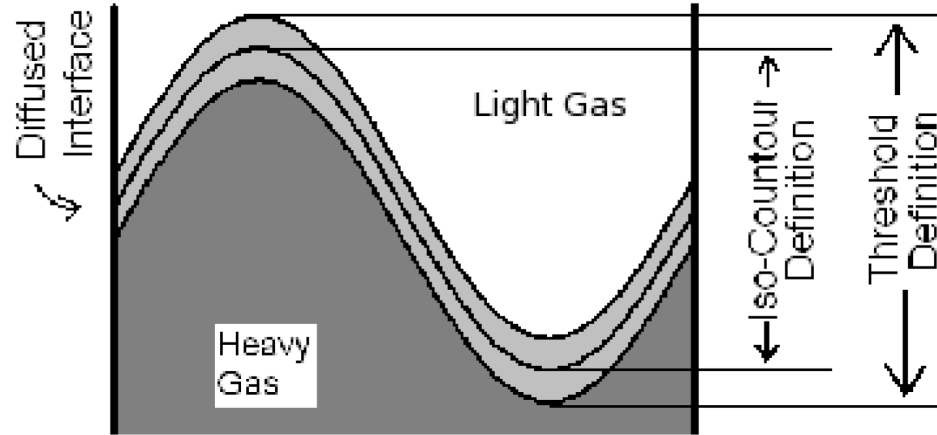


Figure 4.1: Difference between Iso-Contour and Threshold Mixing Length Definition [20].

which $(x) > h$, where (x) is calculated according to the equation below [4]:

$$(x) = 4hY_{SF_6}i(1 - hY_{SF_6}i): \quad (4.21)$$

where $h i$ represents a two-dimensional planar average. This definition is used by [4]. It is extremely dependent on the threshold value h . If the threshold value h is set to 0.95, as done by [4], the gas curtain is measured as the shock-wise distance in the flow where the SF_6 mass fraction is between 39% and 61%. Furthermore, the nature of Equation 4.21 indicates that (x) is extremely sensitivity to perturbations in SF_6 mass fraction, which numerically will lead to drastic jumps in curtain width calculations over time. For these reasons, this method has not been chosen for use in the current work.

A more intuitive definition of gas curtain width, derived from the threshold mixing length method, defines the gas curtain width as the shock-wise distance where $Y_{air} < 1$ [8, 7, 31]. Past studies have used differing values. In this study, the threshold gas curtain definition will be used and will be set to 0.01, so that the gas curtain width is defined as where $Y_{air} < 0.99$. This definition was used because it produces comparable results to previous studies [4, 31, 8, 7], and is naturally intuitive.

4.4 Molecular Mixing Calculation

Once vorticity is deposited to the gas curtain's interfaces, mixing occurs between the two species molecules. In addition to the primary vortices generated, as the mixing layer continues to evolve it develops secondary instabilities along the interface, due to shear interactions, that induce molecular mixing [10, 26]. The mixing length and curtain width quantities previously defined provide only an understanding of the entrainment mixing processes occurring, lending no information on how well-mixed the two fluids are on a molecular level [3, 10]. For this reason, the mixing between the two species molecules can be quantified using the molecular mixing fraction presented below.

$$= \frac{\overline{h Y_1 Y_2}}{\overline{h Y_1} \overline{h Y_2}} dx \quad (4.22)$$

where \overline{h} represents a two-dimensional planar average, and Y_1 and Y_2 are the mass fractions for the two species in the domain. The integral is performed over x values where Y_{SF_6} is first greater than zero, to where Y_{SF_6} first becomes unity, essentially resulting in integration over the entire stream-wise span of the SF_6 gas curtain. It is common in numerical studies to perform this integration across the entire simulation domain [10, 45, 26, 46], however this study follows [3]'s methodology by restraining the integration to the mixing width, so that the result is not skewed by the homogeneity in the rest of the domain. Notice that if the two fluids are completely mixed, the result is unity, whereas if the two fluids are completely separate, the result equals 0, indicating a state of no molecular mixing. The result is only defined in the mixing layer region (if either Y_h or Y_l is zero, the result is $\frac{0}{0} = \text{undefined}$). Therefore, the result quantifies how mixed the two species are on a molecular level within the mixing layer of the gas curtain. This measure has been widely used in literature [3, 10, 31] because it is non-dimensional and provides more information about the degree of mixing present within the mixing layer. Equation 4.22 will be used to calculate the molecular mixing that is occurring for each test case.

4.5 Domain Definition

The domain is defined to represent a two-dimensional channel, containing periodic wall boundary conditions in the transverse directions and a reflecting wall in the x-direction. This can clearly be seen in the schematic presented in Figure 4.2 [3]. The dimensions of

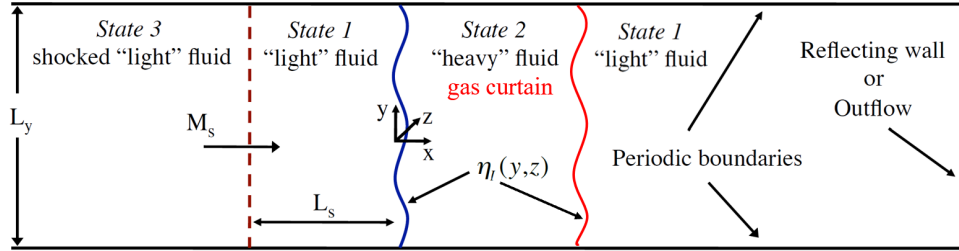


Figure 4.2: Domain Definition Schematic sourced from [3].

the domain for the current work's test cases are defined to be 16 cm and 1 cm in the x- and y-direction respectively, equivalent to the dimensions used by [20, 9, 25]. In order to prove the validity of the numerical simulation, a different two-dimensional domain will be used to reproduce past experimental and numerical results for gas curtain instabilities, defined in the coming section.

The boundary conditions are essential to solving the system of PDEs created by the Navier-Stokes equations. In particular, the boundary conditions in this problem allow the right derivatives and fluxes to be calculated in the ghost layer cells that surround the domain of interest, enforcing the correct conditions on the boundary of the actual domain. Each boundary condition (BC) used is justified below.

4.5.1 Supersonic Inflow

A shock is initialized in the flow using the Rankine-Huginiot equations in order to create the "state 3" conditions found in Figure 4.2. The Rankine-Huginiot equations are as follows:

$$\frac{P_1}{P_0} = 1 + \frac{2}{\gamma + 1} (M_s^2 - 1) \quad (4.23)$$

$$\frac{\rho_1}{\rho_0} = \frac{(\gamma + 1) M_s^2}{2 + (\gamma - 1) M_s^2} \quad (4.24)$$

$$M_1 = \left[\frac{1 + \frac{1}{2}(\gamma + 1) M_s^2}{M_s^2 - \frac{1}{2}(\gamma - 1)} \right]^{\frac{1}{2}} \quad (4.25)$$

where γ is constant due to the calorically perfect gas assumption, and P_0 , T_0 , and M_s are initialized by the user. Defining $u_s = M_s c_0$, where c_0 is the speed of sound at ambient conditions, leads to $u_1 = M_1 \frac{P_1}{\rho_1}$. The post-shock velocity is defined to be $u = u_1 - u_s$, setting the initially un-shocked fluids and initial interface velocities to zero.

The "left" boundary in Figure 4.2 is supersonic inflow, making it partially reflective. As a result, the expansion waves produced during initial shock passage through the gas curtain will partially reflect at the left wall, eventually interacting with the gas curtain again. While a more complex non-reflective boundary condition could be used here, the simplest solution is to stop the simulation before this interaction corrupts the results [3]. This solution has been validated in literature [4, 3, 20].

4.5.2 Periodic BC

The periodic BC is applied to the streamwise "top" and "bottom" walls of the domain. Applying this BC to the transverse walls is extremely common for RMI problems because it is mathematically consistent when comparing numerical simulations with theoretical calculations for a single-mode RMI [3]. Furthermore, the periodic boundary condition physically represents the isolation of the growth of a portion of the gas curtain, indicating that this boundary condition represents a physical scenario.

4.5.3 Closed Wall

In order to simulate reshock, the far-wall of the domain is closed, creating a reflecting wall so that the shock wave reflects and re-shocks the gas curtain.

4.6 Grid Definition and Sensitivity Study

It has been shown in previous studies that the mixing layer growth rate during an RMI simulation becomes grid independent at a certain resolution [9, 20, 3], allowing the focus of the grid choice to be more computationally oriented. Furthermore, past numerical studies have indicated that integral measures, such as mixing length, structure width, and mixing fraction calculations, are relatively insensitive to grid definition [4, 7]. Grid sensitivity of the structure width growth rate is checked for the curtain problem set up below. The results of the grid sensitivity study are presented in Figure 4.3. The tested grids are presented in Table 4.1. The initial conditions and shape of the curtain used for the grid sensitivity study

Table 4.1: Grid Sensitivity Study.

| Grid Number | Discretization | Longitudinal Resolution [m] |
|-------------|----------------|---------------------------------|
| 1 | 2048 X 128 | 78.125 |
| 2 | 4096 X 256 | 39.0625 |
| 3 | 8912 X 512 | 19.53125 |

(Case SM-A) are defined in Table 6.2.

The 4096 X 256 grid shows good agreement with a finer grid of 8192 X 512. Therefore, the 4096 X 256 grid has been chosen for use in the proposed objectives. The grid's discretization results in a grid resolution of $3.90625 \cdot 10^{-5}$ m in both unit directions.

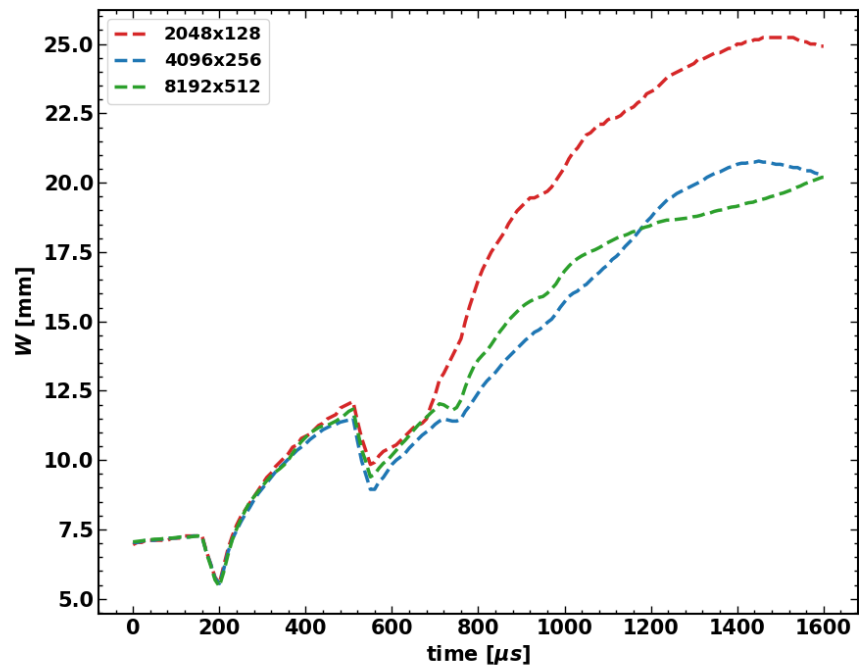


Figure 4.3: Grid Sensitivity of 2D single-mode gas curtain Structure Width W computations.

CHAPTER 5 VERIFICATION

5.1 Single Interface RMI

A simple RMI test case that has well known results was run so that the simulation results could be verified against previous results and empirical models. The test case is a classical RMI between air and SF_6 gas, with the initial flow conditions pictured in Figure 5.1 and tabulated in Table 5.1, and the parameters of the interface's initial geometry tabulated in Table 5.2. The shape of the initial interface was modeled using the equation utilized by Ukai et al. [9] and Leinvet al. [25], presented below.

$$a(y) = a_0 \sin(k_0 y) \quad (5.1)$$

where a_0 and k_0 are the initial interface amplitude and wave number ($k_0 = \frac{2\pi}{\lambda}$). This setup is a reproduction of a case sourced from Ukai. [9]. The current work applied a hyperbolic tangent curve to the initial mass fraction distribution to avoid discontinuities within the grid, according to the equation below.

$$Y_{\text{SF}_6} = \frac{1}{2} + \frac{1}{2} \tanh\left[\frac{(x + a_0 \sin(k_0 y))}{L_p}\right] \quad (5.2)$$

where L_p is the characteristic "thickness" that determines the magnitude of diffusion present around the interface initially, determined based on the grid discretization according to the equation below.

$$L_p = \frac{\text{domain length in streamwise direction}}{\text{discretization in streamwise direction}} \times \text{streamwise grid resolution} \quad (5.3)$$

Figure 5.1: Verification Case Initial Conditions. Initial interface pictured without diffusion modelled.

Table 5.1: Verification Case Initial Conditions $M_s = 1:2$.

| State | Species | Pressure [Pa] | Temperature [K] |
|-------|-----------------|---------------|-----------------|
| 1 | Air | 101,325 | 300 |
| 2 | Air | 153,305 | 338 |
| 3 | SF ₆ | 101,325 | 300 |

Table 5.2: Verification Case Interface Initial Geometry.

| a_0 [mm] | [mm] | Discretization |
|------------|------|----------------|
| 0.5 | 1 | 2048x128 |

The empirical models presented in Equation 2.5 and Table 2.1, and data from Ukai et al. [9], are plotted along side the current setup results for the verification case in Figure 5.2. The numerical results of the current set up follow the results of Ukai et al. [9] very closely during the early time growth, with slight deviations occurring once the growth rate becomes weakly non-linear. These late-time discrepancies are a direct result of the differences in mixing length calculation methods. Ukai et al. [9] uses the threshold method whereas the current setup utilizes the integral method, defined in Equation 4.19. Additionally, no information is provided by Ukai et al. [9] on the methods used to avoid discontinuities in the initial mass distributions. The characteristic thickness used to avoid discontinuities directly effects the growth of the mixing layer because it alters the density gradient present through the interface initially, thus altering vorticity generation. Similarly, the empirical

Figure 5.2: Comparison with 2D Empirical Models and Ukai et al. [9]. Mixing Length is normalized by first subtracting the post-shock mixing length, and then dividing this difference by the initial mixing length.

models under-predict the mixing length growth rate because these models neglect the diffusion thickness, using the iso-contour definition properly defined in Figure 4.1. More significantly, these models were also developed using potential flow theory [14, 18, 16, 19].

This test exemplifies that the current setup results are in accordance with both the results of Ukai et al. [9] and the empirical models [14, 18, 16, 19]. Note that validation of the post-reshock growth rate has not been performed in this work since the empirical models are not widely validated, and numerical results depend highly on the numerical formulations used [9].

5.2 Reference Cases

While the previous verification test indicates that the numerical set-up provides reasonable results for a RMI, further verification of the numerical set-up must be performed because of the additional levels of complexity that gas curtain instabilities contain. Therefore, to ensure that the numerical set-up produces reasonable results for a gas curtain instability, past experimental and numerical studies were simulated numerically, and the results compared.

5.2.1 Balakumaret al. Case Definition [8]

As discussed in the Literature Review, Balakumaret al. [8] obtained the first experimental PLIF images of a SF_6 gas curtain accelerated by a shock wave by using acetone ($\text{C}_2\text{H}_6\text{O}$) as a tracer. PLIF images were taken at the 2 in. plane in the shock-tube domain [8]. Balakumaret al. used the shock tube depicted in Figure 5.3, where the nozzle that creates the SF_6 curtain is a sterolithographically manufactured nozzle which utilizes co-flow in order to avoid vorticity developing on the upstream and downstream interfaces of the curtain. The shock tube pictured in Figure 5.3 is a horizontal shock tube with a 3 in.

Figure 5.3: Experimental Shock Tube used by Balakumaret al. [8]

square cross-section that uses nitrogen as the driver gas and air as the driven gas [8]. A Mach 1.2 shock wave is generated through rupturing of a polypropylene diaphragm that

initially separates the nitrogen and air. The nozzle used is depicted in Figure 5.4, which consists of a row of 21 cylindrical holes of 3.0 mm diameter and 3.6 mm separation that extends across the width of the shock tube. The experimental results for gas curtain width from [8]'s experiment are plotted in Figure 5.6.

Figure 5.4: Experimental Nozzle used by Balakumar et al. [8]

Initial Condition Approximations

Due to natural diffusion occurring and limited data acquisition methods, there are uncertainties in the initial conditions of the $\text{SF}_6\text{-C}_3\text{H}_8\text{-O}$ curtain. In an attempt to approximate the initial conditions, Balakumar et al. [8] used Mikaelian's [33] equation below:

$$I = \frac{A(1 + B \cos(ky))}{1 + B} e^{-x^2/2(1 + \cos(ky))^2} \quad (5.4)$$

where I is the intensity of the light displaced by the acetone molecules, captured by the PLIF cameras. The parameters in Equation 5.4 were approximated by Balakumar et al. [8]. However, Balakumar et al. did not provide any means to convert the intensity curve into mass fractions of the three species within the domain (SF_6 , C_3H_8 , and acetone). Due to this ambiguity, Gowardhan et al. [4] and Shankar et al. [7] each approximated the initial conditions differently in order to reproduce the experimental findings of Balakumar et al. numerically.

Initial Conditions of Gowardhan et al. [4]

Gowardhan et al. converted the intensity curve, Equation 5.4, into air SF_6 mass fractions (neglecting the presence of acetone altogether) by assuming that the intensity at a certain point in the domain was equivalent to SF_6 concentration at that point normalized by the maximum SF_6 concentration occurring in the measurement plane (in.):

$$I = \frac{C_{\text{SF}_6}}{C_{\text{max}}} \quad (5.5)$$

Gowardhan varied the value of C_{max} in order to reproduce Balakumar's findings. The computed curtain width results for the two-dimensional simulations of Gowardhan for C_{max} values of 0.3 and 0.8, are plotted in Figure 5.6 below.

Initial Conditions of Shankar and Lele [7]

Shankar and Lele [7] claimed that the presence of acetone could not be ignored during simulation, converting the intensity curve provided by Balakumar into a curve for the "heavy" gas mass fraction, where the "heavy" gas mass fraction is the sum of the acetone and SF_6 mass fractions. This conversion was done by adjusting the parameters within Equation 5.4. Shankar and Lele tested three different heavy gas initial mass distributions, tabulated below. The results of Shankar's and Lele's three-dimensional simulations for the three test

Table 5.3: Shankar and Lele tested Initial Peak Mass Fractions for Acetone and SF_6 .

| Case | Y_{SF_6} | $Y_{\text{C}_3\text{H}_6\text{O}}$ |
|------|-------------------|------------------------------------|
| 1 | 0.70 | 0.10 |
| 2 | 0.70 | 0.14 |
| 3 | 0.80 | 0.14 |

cases are plotted in Figure 5.6.

Current Work's Initial Conditions

The current work followed Shankar's and Lele's [7] methods to numerically reproduce the initial conditions of Balakumar's [8] experiment. Maintaining a grid resolution of 0.00625 microns, the two-dimensional grid domain was defined to be 0.2 meters in the shock-wise (x) direction and 0.02 meters in the span-wise (y) direction. The initial gas curtain was centered at $x = 0$ meters by defining the grid to span from -0.1 to 0.1 meters and using Equation 5.4. Two sets of parameters for Equation 5.4 were created to provide equations for the initial mass distributions of acetone and SF_6 in the domain, allowing the initial mass distribution of air to be obtained by subtracting the sum of these two equations from unity. Sample initial mass distribution equations for acetone and SF_6 are presented below, respectively:

$$Y_{\text{C}_3\text{H}_8\text{O}} = \frac{0.14(1 + 0.2 \cos(1745y))}{1 + 0.2} e^{-x^2/0.836^2 - (1 - 0.04 \cos(1745y))^2} \quad (5.6)$$

$$Y_{\text{SF}_6} = \frac{0.80(1 + 0.2 \cos(1745y))}{1 + 0.2} e^{-x^2/0.836^2 - (1 - 0.04 \cos(1745y))^2} \quad (5.7)$$

Note that the peak initial mass fractions of acetone and SF_6 can be manipulated by changing the A coefficient in the above equations, where the current sample equations peak initial mass fractions of acetone and SF_6 of 0.14 and 0.80 respectively. Superimposing these equations provides the initial mass distribution of the 'heavy' gas, visualized below in Figure 5.5. The initial heavy gas mass distribution resembles the PLIF image taken by Balakumar et al. of the experimental initial conditions [8]. Simulations were run using the current work's numerical set-up for the initial peak mass fractions of acetone and SF_6 and tabulated below. The results are plotted in Figure 5.6 for comparison.

Figure 5.6 indicates that the current simulation produces acceptable results for gas curtain instabilities, producing mixing length values that are in accordance with the experi-

Figure 5.5: Visualization of initial heavy gas mass distribution used by the current work to numerically reproduce the experimental findings of Balakumara et al. [8], viewed normal to the z-axis. Note that the grid lines merely provide further visualization of the curtain's geometry and do not represent the computational grid.

Table 5.4: Current Work tested Initial Peak Mass Fractions for Acetone and SF₆

| Case | Y_{SF_6} | $Y_{\text{C}_3\text{H}_6\text{O}}$ |
|------|-------------------|------------------------------------|
| 2 | 0.70 | 0.14 |
| 3 | 0.80 | 0.14 |

mental results of Balakumara et al. [8], and the numerical results of Gowardhan et al. [4] and Shankar et al. [7].

Note that matching the experimental results perfectly is impossible due to the ambiguity present in the reported initial conditions of the experiment [8, 4]. In the experiment, the heavy gas has a non-zero velocity in the z-direction, which is unknown and not modelled in the current simulation [8, 4]. Additionally, it is known that the inherent difficulty present in positioning the PLIF camera leads to optical distortions that corrupt intensity measurements [4]. Ultimately, these challenges lead to the precise compositions of air and acetone being unknown [1, 4]. Differences in the current simulation results from the re-

Figure 5.6: Current Simulation Results for Curtain Width, compared to available experimental [8] and numerical data [7, 4]. Curtain width is plotted as difference between the curtain width values and the post-shock curtain width ΔW

sults of Gowardhan et al. are most likely due to the differences in initial mass distributions. Most notably, Gowardhan et al. neglected the presence of acetone all-together, giving rise to substantially different density gradients in the domain [4]. Furthermore, Gowardhan et al. used the curtain width definition defined by Equation 4.21 [4]. Slight differences in the results of Shankar and Lele [7] and the current simulation results could be due to differences in mixing width calculations. No information is provided on the methodology used by Shankar and Lele to compute the mixing width [7]. Note that each comparable current simulation curve and Shankar and Lele curve match closely at early time values. As time goes on, the deviation growth between these curves resembles that of the deviation growth found between the current work's results and Ukai's [9] results for the verification case, presented earlier in Figure 5.2, suggesting that the differences found in Figure 5.6 are due to differences in mixing width computational methods as well. Furthermore, Shankar

al. [7] performed three-dimensional simulations whereas the current simulation performed two-dimensional simulations. The current simulation results presented in Figure 5.6 indicate that the current work's numerical set-up is capable of producing reasonable results for gas curtain instabilities.

5.2.2 Balasubramania et al. Case Definition [31]

Balasubramania et al. [31] performed an experimental study of gas curtain instabilities using the same experimental set up as Balakrishna et al. [8]. However, [31] extended the study of [8] by testing differing nozzle configurations in order to study the effect of initial curtain geometry on the curtain growth, defined in Table 5.5. In Table 5.5, the physical parameters are defined in Table 5.5: Experimental initial conditions sourced from [31] that vary initial curtain shape.

| Case | δ_0 (mm) | λ_0 (mm) | δ_0 (mm) $^{-1}$ | $\delta_0 \lambda_0$ |
|---------------|-----------------|------------------|-------------------------|----------------------|
| SM-1 (short) | 3 | 3.6 | 1.744 | 5.23 |
| SM-2 (long) | 3 | 7.2 | 0.872 | 2.62 |

shape of the nozzles are defined in terms of the nozzle's amplitude and wavelength δ_0 . Balasubramania et al. characterized the shape of a gas curtain by its root-mean-square slope $\delta_0 = \frac{\delta_0}{\lambda_0}$, where $\delta_0 = \frac{2}{\lambda_0}$ [31]. Cases SM-1 and SM-2 represent single mode gas curtains sharing the same thickness, with a short wavelength and long wavelength, respectively. In order to represent these initial conditions mathematically, Balasubramania et al. utilized Equation 5.4 and provided the necessary parameters for each case, tabulated in Table 5.6 [31]. Due to the high degree of uncertainty in initial mass distributions of species, the peak mass fractions for SF_6 and $\text{C}_3\text{H}_6\text{O}$ were kept equivalent to the values used to match the experimental findings of [8], altering them from the provided values of [31]. The initial conditions can be visually compared in Figure 5.7, where it is evident that only a change in wavelength is present between the cases. Note that case SM-1 is numerically equivalent to the reference case current-work simulation for the SF_6 $\text{C}_3\text{H}_6\text{O}$ case, plotted in Figure 5.6 as the pink curve. These parameters will produce the initial condi-

Figure 5.7: Visualization of initial SF_6 gas mass distribution for Case SM-1 and SM-2, respectively, viewed normal to the z-axis. Note that the grid lines merely provide further visualization of the curtain's geometry and do not represent the computational grid.

Table 5.6: Scaled Parameters to mathematically represent the initial conditions presented in Table 5.5. Note that only the wavenumbers differ between cases.

| Case | $A_{\text{SF}_6}=A_{\text{C}_3\text{H}_6\text{O}}$ | B | $k \text{ (mm)}^{-1}$ | | |
|------|--|-----|-----------------------|-------|-------|
| SM-1 | 0.80/0.14 | 0.2 | 1.744 | 0.836 | -0.04 |
| SM-2 | 0.80/0.14 | 0.2 | 0.872 | 0.836 | -0.04 |

tions visualized in Figure 5.7 by using Equation 5.4. The results of these two test cases are plotted in Figure 5.8, which includes the experimental results of Balasubramanian [31]. Comparing the current simulation results to those of [31], it can clearly be seen that despite substantial differences in curtain width values, the trends are preserved. The initial conditions parameters provided by [31] contain errors due to limited data acquisition methods [31, 4]. Furthermore, it is unclear what time $t=0$ in [31]'s data represents. Despite the differences, the current simulation accurately predicts the relationship between initial curtain wavelength and mixing width growth. That is that an increase in wavelength increases the mixing width growth rate [31, 4]. Analogous to Richtmyer-Meshkov behavior, as the initial curtain wavelength is decreased, the deposited vorticity causes the developing bubbles and spikes to carry more lateral motion, dampening the growth of the curtain in time [9, 31, 4].

By reproducing the experimental results of two previous gas curtain studies, it is evident that the current work's simulation set up produces reasonable results for gas curtain

Figure 5.8: Current Simulation Results for SM-1 and SM-2 Curtain Width, compared to available experimental data [31]. Curtain width is plotted as difference between the curtain width values and the initial curtain width γW

instabilities.

CHAPTER 6

RESULTS AND DISCUSSION

Several test cases were defined in order to meet the objectives of the current work. These test cases vary the initial geometry utilizing the equations from [9] and [25], simulating a gas curtain that could be produced experimentally using polypropylene membranes. A basic schematic of the simulation domain is shown below in Figure 6.1. Note that the

Figure 6.1: Basic Schematic of Simulation Domain.

curtain initial temperature and pressure are equivalent to that of the surrounding un-shocked air. This was held true throughout simulation because in a physical experiment, differing initial temperatures between these species would be extremely difficult to create, maintain, and measure. The simulation must resemble what is physically possible in order to ensure that the results are relevant and reproducible experimentally.

The initial conditions for single-mode in-phase curtains are defined as [9, 25]:

$$a(y) = a_0 \sin(k_0 y + \phi) \quad (6.1)$$

where $a(y)$ defines the shape of the upstream and downstream interfaces that form the curtain,

a_0 is the initial amplitude of each interface,

$$k_0 = \frac{2}{\Delta y}$$

is the initial wave number, and ϕ_0 is the phase shift, fixed to $\frac{3\pi}{2}$. The multi-modal curtain shapes were generated through the superposition of multiple wavelengths [25, 20, 9]:

$$a(y) = \frac{a_0}{\sqrt{N}} \sum_{k_y=1}^{k_y^{\max}} [a_{1;k} \cos(\frac{2 k_y y}{L_y} + \phi_{1;k}) + a_{2;k} \sin(\frac{2 k_y y}{L_y} + \phi_{2;k})] \quad (6.2)$$

where k_y is the wavenumber in the y-direction, $a_{i;k}$ are random coefficients between -1 and 1, $\phi_{i;k}$ and $\phi_{j;k}$ are random coefficients between 0 and 2π , L_y is the domain size in the y-direction, and \sqrt{N} is the standard deviation of the summation part to normalize the fluctuation to be one, and the initial amplitude a_0 determines the size of the perturbation.

Using the hyperbolic tangent to avoid discontinuities in initial mass fraction distributions, these interfaces were superimposed to form the curtain by shifting one interface further downstream, using the equation below.

$$Y_{SF_6} = \frac{1}{2} [\tanh[\frac{(x + a(y) + \Delta x)}{L_p}] + \tanh[\frac{(x + a(y) + \Delta x + \Delta x)}{L_p}]] \quad (6.3)$$

where Δx is defined as the curtain thickness in this study, and Δx is a parameter that shifts the curtain to be centered at $x = 0$. Δx must be calculated for each change in curtain thickness by setting the derivative of Equation 6.3 to zero at $x=0$ and $y = \frac{L_y}{2}$:

$$0 = \frac{1}{2L_p} [\text{sech}^2(\frac{(x + a(y) + \Delta x)}{L_p}) - \text{sech}^2(\frac{(x + a(y) + \Delta x + \Delta x)}{L_p})] \quad (6.4)$$

L_p , which determines how diffuse the two interfaces are, was fixed to the grid resolution to avoid it affecting the results. As mentioned previously, a change in L_p would result in changes in the density gradient across the interfaces (different diffusion layers), leading to

different mixing if this parameter was varied between cases. The current work chose to model a gas curtain using the above methodology over utilizing Equation 5.4, which represents gas curtains experimentally created using nozzles, because varying the wavelength and amplitude of the gas curtain is far more straightforward using the latter. More importantly, changing any parameter within Equation 5.4 results in changes to the diffusivity of the gas curtain, making the isolation of shape parameters' effects on the curtain growth difficult. Using the equations above to define the curtain ensures that the diffusivity between initialized curtains is preserved, ensuring that a shape parameter's effect on curtain growth is in-fact isolated. A sample surface plot of the initial SF_6 mass fraction distribution is provided in Figure 6.2 for Case SM-a, defined later.

Figure 6.2: Initial Conditions Visualization for Case SM-a. Note that the grid lines merely provide further visualization of the curtain's geometry and do not represent the computational grid.

6.1 Single Shock Studies

Before re-shock conditions can be studied, it is important to have a firm understanding of the behaviors of gas curtain instabilities to a single shock passage. Towards this end, the following section performs a quick study of singularly shocked gas curtains, comparing the current work's results to available results found in literature.

6.1.1 Single Mode Shape Study

Four single mode curtain cases, tabulated in Table 6.2, were defined that test both Balasubramanian et al. [31] ($B = a_0 \frac{2}{\lambda_0}$) and Gowardhan et al. [4] ($G = w_0 \frac{2}{\lambda_0} = w_0 k_0$) root-mean-square slope characterizations of gas curtains, discussed in the literature review chapter of the current work. Recall that w_0 , λ_0 , and k_0 are the curtain's initial amplitude, thickness, wavelength, and wavenumber respectively. Note that Case A is a single-interface RMI with the same interface initial conditions as the curtain case SM-A. The grid resolu-

Table 6.1: Single Mode Shape Study Test Cases.

| Case | M_s | P_1 [Pa] | T_1 [K] | a_0 [mm] | λ_0 [mm] | w_0 [mm] | B | G |
|----------------|-------|------------|-----------|------------|------------------|------------|---------|--------|
| A ⁰ | 1.5 | 101,325 | 300 | 0.50 | 5 = 18 | 0 (RMI) | 5 = 36 | NA |
| SM-A | 1.5 | 101,325 | 300 | 0.50 | 5 = 18 | 6 | 5 = 36 | 5 = 3 |
| SM-B | 1.5 | 101,325 | 300 | 1.00 | 5 = 18 | 6 | 5 = 72 | 5 = 3 |
| SM-C | 1.5 | 101,325 | 300 | 0.50 | 5 = 36 | 6 | 5 = 72 | 5 = 6 |
| SM-D | 1.5 | 101,325 | 300 | 0.50 | 5 = 72 | 6 | 5 = 144 | 5 = 12 |

tions relative to the initial wavelengths of the curtains are tabulated below for each case. These cases represent low-wavelength single-mode cases, resulting in the lowest amount

Table 6.2: redSingle Mode Shape Study Test Cases.

| Case | λ_0 [mm] | $X = \lambda_0$ |
|------|------------------|-----------------|
| SM-A | 5 = 18 | 22 |
| SM-B | 5 = 18 | 22 |
| SM-C | 5 = 36 | 11 |
| SM-D | 5 = 72 | 6 |

of grid points per wavelength ($X = \lambda_0$) simulated throughout this study. However, the grid

resolution per wavelength is shown to be acceptable based on the grid resolution study performed earlier for Case SM-A (Figure 4.3). The mixing width results for SM-A through SM-D are plotted in Figure 6.3 below. For Cases SM-A through SM-D, it is found that the

Figure 6.3: Single Mode Gas Curtain Growth Results, structure width and time are normalized by their respective value immediately following shock passage (δ_0 and M_0^+).

higher the initial δ_0 (larger δ_0) leads to larger gas curtain width growth in time, which is consistent with the findings of [4] and [31]. Recalling the results presented in Figure 5.8, this trend can be explained from a vortex dynamics perspective. That is, as the initial wavelength of the gas curtain decreases, opposite vortices developing, due to the baroclinic torque generation upon shock passage, become closer in space, leading to interactions between these competing vortices sooner in time. These interactions lead to less mixing width growth over time [9, 4, 31]. Earlier bubble merger and competition processes leads to more lateral (span-wise) interface perturbation growth, which does not contribute significantly to stream-wise growth of the curtain width [9]. Essentially, a decrease δ_0 inhibits the free

space a bubble has to grow, diminishing the entrainment process described previously.

Notice that there are insignificant differences in curtain growth rates between cases SM-A and SM-B, which only differ in initial amplitude. Two additional test cases were defined with differing initial perturbation amplitudes. The two cases defined in Table 6.3 are

Table 6.3: Single Mode Amplitude Study Test Cases.

| Case | M_s | P_1 [Pa] | T_1 [K] | a_0 [mm] | r_0 [mm] | w_0 [mm] | B | G |
|----------|-------|------------|-----------|------------|------------|------------|--------|-------|
| SM-amp1 | 1.5 | 101,325 | 300 | 0.01 | 5 = 18 | 6 | 5 = 36 | 5 = 3 |
| SM-amp10 | 1.5 | 101,325 | 300 | 0.1 | 5 = 18 | 6 | 5 = 72 | 5 = 3 |

plotted in Figure 6.4. From Figure 6.4, it can be seen that the growth rate is proportional

Figure 6.4: Variation of initial amplitude effect on gas curtain instabilities.

to the perturbation amplitude. Increasing the initial amplitude of the curtain's interfaces increases the amount of baroclinic torque being generated, due to the added surface area of the interface that is misaligned with the impinging shock. This increase in vorticity leads to an increase in the structure width growth rate, aiding the entrainment process. However,

the effect of varying the amplitude is diminished by the interactions between the curtain's interfaces. The bubble growth of the upstream interface is inhibited by perturbation growth of the downstream interface. Furthermore, the phase-inversion process (of a heavy-light RMI configuration) of the downstream interface is inhibited by the bubble growth of the upstream interface. With only a finite amount of heavy fluid (ρ_6) to join in the entrainment process, the upstream and downstream interfaces must compete to draw the heavy fluid into their structures. Additionally, wave reverberations oscillating off the interfaces redistribute vorticity (through further baroclinic torque generation) through the growing mixing layer. These interactions between the interfaces diminish the ramifications of a change in initial amplitude, when compared to single-interface RMIs. This is most likely why [4]'s characterization of gas curtain's does not account for changes in amplitude. However, clearly large changes in amplitude do still effect the curtain's structure width growth rate, revealing a weakness of [4]'s characterization method.

It is interesting to compare the molecular mixing of the cases presented in Table 6.2 using the molecular mixing fraction defined in Equation 4.22, plotted for each case in Figure 6.5. Before the differences in values for the cases are discussed, it is important to discuss the shared behaviors, in order to understand the behavior during the gas curtain instability growth. Plotted versus the raw time of the simulation in Figure 6.5, the shock wave does not impact the upstream interface of the curtain until approximately 160 microseconds. Notice that for all cases however, significant increases occur before even the upstream interface is shocked (from 0 to 150 microseconds). This increase is due to molecular diffusion across the interface between the two species [26]. Such diffusion is depicted in the contour snapshots found in Figure 6.6 below. As time progresses, molecular diffusion is evident with the growth of the "purple" layer present in Figure 6.6. Notice that as the wavelength₀ is decreased, experiences more growth before shockage of the curtain. This result is expected because a decrease in λ_0 causes an increase in the interface's surface area, providing more area for molecular diffusion to occur. An increase

Figure 6.5: Single Mode Molecular Fraction Results for Cases defined in Table 6.2.

in the initial amplitude initializes more heterogeneity in the domain, explaining why the lower amplitude SM-B case begins with a higher compared to SM-A.

The shock passage through the upstream interface causes the initial rapid decrease in ϕ , due to the diffusion layer being compressed. Immediately once the shock leaves the upstream interface, ϕ increases rapidly due to the growing perturbations that grow the mixing layer. Around approximately 200 microseconds, the downstream interfaces of the curtains are shocked, leading to the pulse in seen in Figure 6.5. SM-D's transient response to the shock passage differs from the other cases due to its high initial value, where it almost reaches unity. The "pulses" observed, and behavior of Case SM-D indicate the high degree of sensitivity ϕ has to a shock passing through the curtain's interfaces [45]. ϕ is highly sensitive to molecular diffusion due to its definition, mainly in the manner in which it is non-dimensionalized [45]. Due to the sensitivity of ϕ during shock passage, comparing the behaviors of ϕ 's values for differing cases during this period of time is extremely difficult.

Figure 6.6: Contour Plots of SF_6 mass fraction for case SM-C, used to visualize the molecular diffusion occurring across the upstream interface before shock passage (shock reaches curtain upstream interface at approximately 140 s). From left to right: $t = 0$ s, $t = 40$ s, $t = 140$ s.

For this reason, the trends of following shock passage will only be discussed, mainly the asymptotic values reached. The asymptotic values indicate the level of mixedness achieved within the mixing layer of the curtain.

Notice that the period of decreasing after the shock passes through the entirety of the curtain (200–220 s) is significantly shortened compared to this period during single-interface RMIs (see [10], [26]). Logically, this must be due to the interactions between the interfaces. The entrainment competition between interfaces inhibits bubble and spike growth, reducing the main cause for a decrease observed in single-interface RMIs [10]. Recall that for a single-interface RMI, bubble and spike growth decreases because their growth involves asymmetrical entrainment of the heavy fluid, resulting in more heterogeneity in the flow [10, 45]. Referring to the curtain (Figure 6.5), as the perturbations on the interfaces grow, the vorticity on the downstream side of the upstream interface and the upstream side of the downstream interface interact, disrupting the bubble and spike

formation within the curtain structure. This disruption of large-structure growth within the curtain must lead to an increase in Physically this is also intuitive, because the vortex structures (responsible for the entrainment process) lose their stream-wise orientation due to interface interactions, not only inhibiting spike and bubble growth, but also resulting in the inside of the curtain reaching a more mixed state, thus increasing (see Figure 6.8 and Figure 6.9). This scrambling is exacerbated by the wave reverberations occurring within the curtain as well. Each reverberated wave is physically a pressure gradient, that when passing through the developing structures, generates further baroclinic torque over a wider range of scales.

Notice that a decrease in the initial wavelength increases the asymptotic value of Furthermore, Figure 6.5 clearly shows that a smaller leads to greater molecular mixing growth. This result is consistent with the curtain width results presented in Figure 6.3. As the interface's initial wavelength (λ_0) is decreased, more vorticity is deposited to the interface after shock passage due to the nature of baroclinic torque generation. From the curtain width perspective, this added vorticity works to slow down curtain growth because the vortex pairs compete sooner in time as λ_0 decreases, inhibiting the entrainment process. From a molecular mixing perspective, this increased deposition of vorticity, coupled with the increase in vortex interactions at earlier times, leads to greater molecular mixing [31]. The earlier vortex interactions lead to the vortex pairs becoming scrambled. As noted by [4] and [9], this scrambling mainly occurs in the transverse direction, which explains why the curtain width measure fails to capture this phenomenon.

6.1.2 SingleModeCurtainThicknessStudy

Further test cases are defined in Table 6.4 that vary the curtain thickness. Cases presented in Table 6.4 are plotted in Figure 6.7a and Figure 6.7b for curtain width and mixing fraction results, respectively. Notice that in the early time after shock passage, the greater initial curtain thickness case (SM-H) experiences linear growth for a longer period. This is due to

Table 6.4: Single Mode Curtain Thickness Study Test Cases.

| Case | M_s | P_1 [Pa] | T_1 [K] | a_0 [mm] | o_0 [mm] | w_0 [mm] | B | G |
|------|-------|------------|-----------|------------|------------|------------|---------|--------|
| SM-A | 1.5 | 101,325 | 300 | 0.50 | 5 = 18 | 6 | 10 = 36 | 5 = 3 |
| SM-G | 1.5 | 101,325 | 300 | 0.50 | 5 = 18 | 1 | 10 = 36 | 10 = 3 |
| SM-H | 1.5 | 101,325 | 300 | 0.50 | 5 = 18 | 24 | 10 = 36 | 5 = 6 |

(a)

(b)

Figure 6.7: Gas curtain growth (a) and (b) results for Cases defined in Table 6.4. In (a) $t = 0$ s corresponds to immediately after shock passage. In (b) $t = 200$ s corresponds to immediately after shock passage.

the fact that the upstream and downstream interfaces are separated by a greater initial distance. With no other parameters changed, the same vorticity is deposited to the interfaces initially. Therefore, the greater initial curtain thickness case experiences "un-inhibited" curtain growth for a longer period of time, because the vorticity deposited to its two interfaces requires a longer period of time to begin interacting. When the vorticity between the interfaces begins to interact, the bubble and spike growth is inhibited, [4, 31], disrupting the entrainment process and thus dampening the curtain growth rate. Furthermore, a decrease in the initial curtain thickness results in less heavy fluid available to join in the entrainment process. Both interfaces must compete for a limited amount of heavy fluid to feed the growth of their structures. This competition slows the growth of each interfaces' structures. It appears however, the effect of curtain thickness on the curtain growth rate becomes less significant as the curtain thickness gets smaller. The effect of initial curtain

thickness on the curtain growth after shock passage, that is revealed in Figure 6.7a, agrees with [4]'s findings. As the curtain initial thickness increases, the rms slope of the curtain (σ) increases, supporting [4]'s characterization method for curtain growth prediction. Figure 6.7a shows the deficiency of [31]'s characterization method, which does not account for changes in curtain thickness at all. As the curtain thickness increases, the perturbations on the upstream and downstream interfaces are able to grow in time more independently, and have more heavy fluid available to feed the entrainment process, recovering the classical RMI behavior [31].

This is even more evident in the results presented in Figure 6.7b. Notice that before shock passage, increases equally for all three cases. This is a result of the initial interface perturbations for all cases being equivalent, resulting in the same molecular diffusion. The thick curtain (SM-H) has a very comparable trend to SM-A, where the pulses in due to the shock hitting the upstream and downstream curtains are further apart in time due to the increased initial curtain thickness. At later times however, the asymptotic value of for SM-H is lower than that of SM-A. The thin curtain (Case SM-G) experiences greater growth because stronger interactions between the vorticity deposited to each interface leads to greater mixing of species. Initial curtain thickness is inversely proportional for a gas curtain instability. Increasing the initial curtain thickness allows the bubble and spike growth processes to continue longer in time, driving the entrainment process that leads to growth in the structure width. As the curtain thickness is decreased, the role of vorticity switches from driving asymmetrical entrainment of the heavy fluid, into mixing the species within the curtain. The physical justification for this role-switch is discussed in the following paragraph. Furthermore, with less distance to travel, the wave reverberations travel through the entirety of the thin curtain more frequently, further redistributing vorticity.

These processes can be visualized in Figure 6.8, where contour plots of the vorticity in the z-plane are shown for Cases SM-G and SM-A.

(a) SM-A: $t_0^+ = 0$ s

(b) SM-A: $t_0^+ = 200$ s

(c) SM-G: $t_0^+ = 0$ s

(d) SM-G: $t_0^+ = 200$ s

Figure 6.8: Contour plots of f_z for cases SM-A and SM-G at times after initial shock passage (t_0^+).

Notice that after the shock has left the curtain, the vortex-pair structure, which drives the mixing layer growth through entrainment processes, is present in both curtains. At a later time however, this vortex-pair structure is scrambled in the thin curtain (SM-G), while still preserved in the thicker curtain (SM-A).

More refined steps in time for the thin curtain are shown in Figure 6.9 to understand this scrambling process further. In Figure 6.9, the ordered vortex-pair structure begins to break-down through the merging of vortex tubes between the two interfaces (50 s). The merging of vortical tubes between interfaces draws the large scale vortical motions towards the center of the curtain [47]. Furthermore, the merging process results in the strengthening

of some vortices and the destruction of others [47]. At even later times, most vortex-pair structures have been lost due to the interactions between the curtain's interface. The primary cause of inhibited mixing layer growth, for the cases defined above, is due to the random orientation of the vortical structures that results from interface interactions. Because the orientation of these vortex structures has been scrambled, the asymmetrical entrainment process in the stream-wise direction is lost. The vortex structures still present lead to mixing of the species within the curtain, rather than structure width growth. In Figure 6.10, the diminished entrainment process for the thin curtain SM-G can be seen through comparison with the entrainment process of the thicker curtain SM-A. Notice the much higher concentration of SF_6 present in the mushroom structures of SM-A. Furthermore, the downstream interface's mushrooms for SM-G are oriented in the transverse direction, whereas in SM-A these downstream mushrooms are still oriented in the stream-wise direction. As the curtain thickness increases, the orientation of the vortex pairs are no longer affected by the presence of the other interface, leading to the single-interface RMI behavior being recovered. This can be seen by noticing that the SF_6 structures for SM-H's upstream interface are almost indistinguishable from the structures for the single-interface RMI (Figure 6.11). Together these images reveal the fundamental effect of initial thickness on a curtain's structure width growth and molecular mixing after initial shock passage, given that the initial conditions of the curtain's perturbations are sufficiently complex (to be discussed later).

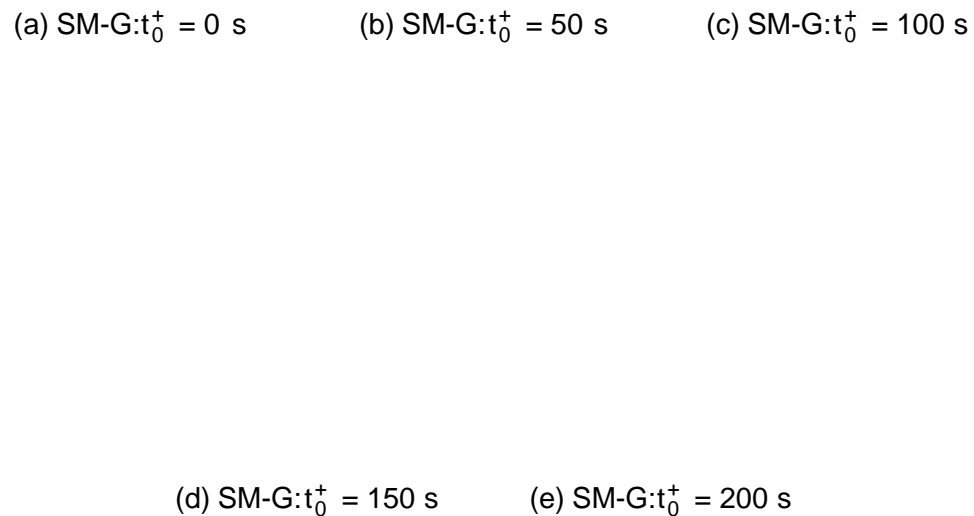


Figure 6.9: Contour plots df_z for cases SM-G at times after initial shock passage (a) (

Analysis of Gas Curtain Characterization Methods

For each test case defined previously, the gas curtain growth rates were computed so that the qualitative characterization methods defined by [4] and [31] could be properly tested, tabulated below Table 6.5. Both characterization methods qualitatively predict the effect of wavelength changes in the initial perturbations. However, [31]'s characterization does not account for changes in gas curtain thickness, whereas [4]'s characterization does not account for changes in amplitude. From the results presented earlier and Table 6.5, it is clear that both of these characterization methods fail to account for all changes in initial conditions that effect the curtain's growth rate.

(a) SM-A: $t_0^+ = 100$ s

(b) SM-G: $t_0^+ = 100$ s

Figure 6.10: Contour plots of χ_{SF_6} for cases SM-G and SM-A.

Table 6.5: Characterization Methods for Gas Curtain Instabilities.

| Case | B | G | dW=dt (m/s) |
|----------|---------|--------|-------------|
| SM-A | 5 = 36 | 5 = 3 | 23.44 |
| SM-B | 5 = 72 | 5 = 3 | 23.08 |
| SM-C | 5 = 72 | 5 = 6 | 18.72 |
| SM-D | 5 = 144 | 5 = 12 | 10.44 |
| SM-amp1 | 5 = 36 | 5 = 3 | 17.40 |
| SM-amp10 | 5 = 72 | 5 = 3 | 23.58 |
| SM-G | 5 = 36 | 5 = 18 | 23.45 |
| SM-H | 5 = 36 | 10 = 3 | 27.81 |

Mikaelian's Model Comparison

As mentioned in the literature review section, Mikaelian's [17] interface velocity model (Equation 2.12 through Equation 2.16) was quickly tested for several initial curtain configurations performed in the current work. For the SM-7 cases (defined in Table 6.10), the peak of the upstream interface was computationally defined as the location at which the SF_6 mass fraction is closest to 50% along the center-line of the domain in the transverse direction (for Cases SM-7-, the interface peak is at the center-line, see Table 6.10). Likewise, the trough of the upstream interface was computationally defined as the location at which the SF_6 mass fraction is closest to 50% $y \neq 0$. The streamwise positions for

(a) A': Initial Conditions. (b) A': $t_0^+ = 100$ s (c) A': $t_0^+ = 200$ s

(d) Upstream Interface of SM-H: Initial Conditions. (e) Upstream Interface of SM-H: $t_0^+ = 100$ s (f) Upstream Interface of SM-H: $t_0^+ = 200$ s

Figure 6.11: Contour plots of ϕ_{SF_6} for cases A' (RMI) and the upstream interface of SM-H (Thick Curtain). Notice that the development of the instabilities are indistinguishable, showing that at sufficiently large curtain thicknesses, the single-interface RMI behavior is recovered.

each peak and trough were recorded for the first 10 time-steps following shock passage. For the SM-A and SM-G cases, the streamwise positions of the upstream interface's peaks and troughs were traced visually within Tecplot. This rudimentary method is acceptable for these two cases for reasons explained in the following paragraph. The jump velocities (v) were taken as the speed of the midpoint between peak and trough, computed using a linear regression. Similarly, the amplitude was computed as half the distance between the

positions of each respective peak and trough, with the amplitude growth rate computed using a linear regression fit to the amplitude versus time data. The results for each case are tabulated in Table 6.6 alongside the predicted growth-rate from Mikaelian's model (model γ) and the percent difference between these values. Only the upstream interface amplitude growth rate was computed because Mikaelian's model predicts the same growth rate, just oppositely signed, for the downstream interface [17].

Table 6.6: Comparison of Mikaelian's Model [17] and the current work's simulation results for the amplitude growth rate of the upstream interface.

| Case | k_0 | v (m=s) | γ (m=s) | Model γ (m=s) | % Diff |
|---------|---------|-----------|----------------|----------------------|----------|
| SM-A | 3.6 | 62.113 | 10.625 | 150 | 173.54 % |
| SM-G | 3.6 | 84.672 | 9.6355 | 204 | 181.96 % |
| SM-7-6 | 0.00001 | 73.704 | 20.543 | 29.93 | 37.20 % |
| SM-7-1 | 0.00001 | 91.761 | 10.866 | 13.3 | 20.14 % |
| SM-7-24 | 0.00001 | 65.075 | 17.099 | 27.47 | 46.54 % |

Notice that for the small wavelength cases (SM-A and SM-G defined in Table 6.4), the model is incapable of predicting the amplitude growth rate. This is expected because Mikaelian's model is limited to small initial perturbations ($k_0 \ll 1$). From Table 6.6, it is clear that this requirement is substantially exceeded. For the SM-7 cases however, this requirement is met. For these cases, it can be seen that Mikaelian's model predicts amplitude growth rates that are comparable to the current work's results. The model seems to be more accurate as the initial curtain thickness decreases. The differences between the model and the current work's results are most likely due to the limitations of the model. Recall that Mikaelian's model [17] ignored compressibility and non-linear effects, assumed sharp interfaces, and did not consider the presence of wave reverberations within the curtain. Most significantly, the assumption of sharp interfaces ignores the diffusion layer surrounding the interface. This diffusion layer has been shown to significantly effect the amplitude growth

rate due to it altering the magnitude and direction of the density gradient, which directly effects baroclinic torque generation [26]. Sharp interfaces lead to stronger density gradients, which would lead to greater amplitude growth rates. This explains why Mikaelian's model over-predicts the amplitude growth rates. Another source of difference between the rates could be due to the definition of the interface edge used by the current work, computationally defined as where the F_6 mass fraction is closest to 50%. This definition was made using an ad-hoc decision, which contradicts Mikaelian's sharp interface assumption. Additionally, the jump velocity computation is slightly incorrect, leading to another source of discrepancy between the rates. Recalling Figure 2.2, the jump velocity is the velocity of the unperturbed interface, which is defined as where the bubble and spike amplitudes meet in the streamwise direction [9]. Because no models or computational methods exist to calculate the bubble/spike amplitude growth rates for gas curtains, the jump velocity was computed as described previously. Used as an input to Mikaelian's model, this erroneously calculated jump velocity leads to further discrepancy between Mikaelian's model and the current work's results. Considering these sources of discrepancies, Mikaelian's model predicts the upstream interface's amplitude growth rate reasonable well compared to the current work's simulations, as long as the small initial perturbation ($\epsilon \ll 1$) requirement is met.

6.1.3 Multi-Mode Shape Study

Two multi-mode cases were defined that are tabulated in Table 6.7, where k_{max} is the number of modes present in the initial perturbation. In order to ensure comparability, the domi-

Table 6.7: Multi-Mode Curtain Shape Study Test Cases.

| Case | M_s | P_1 [Pa] | T_1 [K] | k_{max} | a_0 [mm] | λ_0 [mm] | w_0 [mm] | $X = \lambda_0$ |
|------|-------|------------|-----------|-----------|------------|------------------|------------|-----------------|
| MM-2 | 1.5 | 101,325 | 300 | 2 | 0.50 | $5 = 18$ | 6 | 22 |
| MM-8 | 1.5 | 101,325 | 300 | 8 | 0.50 | $5 = 18$ | 6 | 22 |

nant mode in each case was defined to have an initial amplitude and wavelength equivalent

to the initial values for case SM-A. The curtain width results for cases MM-2 and MM-8 are plotted in Figure 6.12, along with case SM-A for comparison. Figure 6.12 clearly shows

(a) (b)

Figure 6.12: Multi-mode gas curtain growth (a) results and (b) for cases differing in initial number of modes.

that as the number of modes present in the curtain's initial interfaces increases, the curtain growth is dampened. Even the addition of a second mode leads to a significant decrease in curtain growth. This trend is consistent with single-interface RMI behavior [9]. There is an insignificant amount of previous studies that have investigated multi-modal curtains ([31, 4]). However, the vortex dynamics perspective applied to the single mode curtain shape study can be leveraged in the study of multi-modal curtains as well [9]. Logically, modal competition becomes more significant as the curtain becomes more multi-modal [4, 31]. An increase in the number of initial modes present in the curtain's interfaces is analogous to a decrease in the curtain's initial wavelength. As the number of modes is increased, the increased amount of initial perturbations present in the interface leads to vortices being generated that are closer initially in space, leading to them interacting sooner in time. This increased modal competition significantly augments the curtain growth rate [4, 31]. The larger structures have less space to grow, inhibiting the entrainment process [11]. Furthermore, the modal competition occurring causes the dominant structures to gain momentum in the transverse direction.

Before shock passage ($t = 200 \text{ s}$), an increase in the number of modes causes a significant increase in σ due to the increased interface surface area, allowing more diffusion to occur. The shape of SM-A's and MM-2's results are very comparable, whereas the results for MM-8 differ. This is most likely due to the high level of diffusion that occurs before shock passage in case MM-8.

While the behavior during shock passage through the curtain differs between cases, all three cases reach similar asymptotic values of σ . However, the multi-modal cases reach a slightly higher value than the single-mode case, suggesting that the presence of additional modes in the curtain's initial perturbations promote molecular mixing. Holding the curtain thickness fixed, changing the number of modes present in the curtain's interfaces has the same effect as that seen for single-interface RMI's. With more modal competition, the vorticity deposited to the interfaces contribute to molecular mixing more than mixing length growth [9], causing the bubbles and spikes to move more in the transverse direction [20]. The contour plots of σ for MM-2 and MM-8 illustrate the tangential orientation of the bubbles and spikes that additional modes induce (Figure 6.13). Additionally, the inhibition of the bubble and spike growth, caused by the increase in modal competition from the added number of modes, is evident in Figure 6.13 through the comparison of the relative sizes of bubbles and spikes between the cases.

(a) MM-2: $t_0^+ = 70$ s

(b) MM-2: $t_0^+ = 320$ s

(c) MM-8: $t_0^+ = 70$ s

(d) MM-8: $t_0^+ = 320$ s

Figure 6.13: Contour plots of $\frac{\text{kg}}{\text{m}^3}$ for cases MM-2 (TOP) and MM-8 (Bottom).

6.1.4 Multi-Mode Curtain Thickness Study

Two additional cases were defined that vary the initial curtain thickness of cases MM-2 and MM-8, defined below in Table 6.8. The results are plotted below in Figure 6.14.

Table 6.8: Multi-Mode Curtain Thickness Study Test Cases.

| Case | M_s | P_1 [Pa] | T_1 [K] | k_{max} | a_0 [mm] | λ_0 [mm] | w_0 [mm] |
|---------|-------|------------|-----------|-----------|------------|------------------|------------|
| MM-2-24 | 1.5 | 101,325 | 300 | 2 | 0.50 | 5 = 18 | 24 |
| MM-8-24 | 1.5 | 101,325 | 300 | 8 | 0.50 | 5 = 18 | 24 |

(a)

(b)

Figure 6.14: Multi-mode gas curtain growth (a) results and (b) for cases differing in initial thickness.

Figure 6.14 indicates that an increase in initial curtain thickness increases the curtain growth rate after shock passage. This is due to the same reasons mentioned for the single mode curtain thickness study. As the initial curtain thickness increases, the perturbations on the upstream and downstream interfaces of the curtain can grow independently for a longer period of time. It is also worth noting that an increase in initial curtain thickness has a greater effect on curtain growth rates for the multi-mode cases with fewer modes in its initial perturbations. As more modes are added to the initial perturbations, despite independence from the curtain's other interface, the additional modes reduce curtain growth because they add more lateral motion and vortex competition to the perturbation growth, dampening the effect of a change in initial thickness on the mixing layer growth [9, 4, 31].

Consistent with the previous single-mode results, the higher modal cases exhibit much greater declines in χ as the shock traverses the curtain. Because these cases have such high molecular diffusion occurring before shock passage, χ decreases rapidly when the curtain's interfaces are compressed from shock passage. Of most importance from χ results are the differences in asymptotic values for the thicker initial curtains. This result suggests that the initial thickness of the curtain has a larger effect on late-time χ than the number of modes present in the curtain's perturbation. This is most likely due to the bubble and spike structures maintaining their stream-wise orientation into later times for the thicker curtains [9, 20]. The survival of vortex pair structures into later times promote the bubble and spike stream-wise growth that causes asymmetrical entrainment of the fluid, growing the structure width rather than increasing χ [26, 45, 10, 9].

6.2 Reshock Studies

6.2.1 Single Mode Shape Reshock Studies

The above cases were run under re-shock conditions in order to provide novel results that attempt to understand how the initial conditions affect curtain growth post re-shock. A re-shock of a gas curtain is defined as when the reflected shock traverses through the entirety of the curtain. Cases SM-A through SM-D are plotted under reshock conditions in Figure 6.15. The results presented in Figure 6.15 suggest that the post-reshock curtain growth rate is not a strong function of wavelength or amplitude, supporting the claims of [8]. For reference, a sample slope of 19.61 m/s of curtain growth is shown as a black solid line in Figure 6.15. Table 6.9 summarizes the growth rates $\frac{dW}{dt}$ and conditions at reshock for the cases plotted in Figure 6.15. As the curtain structure is re-shocked, the vorticity is re-distributed over a wider range of scales in many directions, leading to similar structure growth rates for all cases [8, 9, 31]. The results further support this finding by showing that for all cases χ reaches similar values. The reshock initially causes a rapid decrease in χ due to the compression of the mixing layer. After the reflected shock has passed,

Figure 6.15: Single Mode Gas Curtain Post-Reshock Growth Results for cases differing in initial shapes (θ_0 and a_0) (Table 6.2).

Table 6.9: Reshock Parameters for Single-Mode Shape Studies.

| Case | a_0 [mm] | θ_0 [mm] | w_r [mm] | r | $\frac{dW}{dt}$ [m=s] |
|------|------------|-----------------|------------|------|-----------------------|
| SM-A | 0.5 | 5 = 18 | 3.42 | 2.98 | 20.65 |
| SM-B | 0.25 | 5 = 18 | 4.12 | 3.60 | 14.94 |
| SM-C | 0.5 | 5 = 36 | 2.76 | 1.20 | 13.71 |
| SM-D | 0.5 | 5 = 72 | 0.91 | 0.20 | 19.61 |

continues to decrease slightly due to the rapid structure width growth that follows after reshock, increasing heterogeneity in the domain. As time goes on, secondary instabilities and the scrambled perturbations eventually result in increasing in time. Because vorticity is deposited over a much wider range of scales during reshock, the curtain's interfaces become well-mixed molecularly, sufficiently scrambled to the point that it seems to become constant no matter the conditions of the initial interface. The additional wave reverberations introduced by re-shock aid this shared asymptotic behavior as well. The asymptotic values of mixed-ness are between 0.7 and 0.8, which are consistent with mixing fraction calculations for reshock RMI studies as well [26, 45, 10, 43]. This consistency is upheld through the rest of the reported results as well, where asymptotic values of mixedness will be shown to vary between 0.6 and 0.9, depending on the initial thickness of the curtain (which will be discussed in depth later).

6.2.2 SingleModeCurtainThicknessReshockStudies

Furthering the studying of gas curtain reshock behavior, cases SM-G and SM-H under reshock conditions are plotted in Figure 6.16. It is clear that the thickness of the curtain

Figure 6.16: Gas Curtain Post-Reshock Growth and Results for cases differing in initial thickness (Table 6.4).

effects the late-time growth of the molecular mixing. The thin curtain (SM-G) reaches a noticeably higher final value of \bar{m} , while cases SM-A and SM-H reach relatively the same value. Referring to Figure 6.10, this is due to the fact that before reshock, the vorticity generated on each interface of the thin curtain has been interacting for a longer period of time. These earlier interactions lead to the the vortical structures becoming scrambled within the thin curtain, which causes greater mixing between species inside the curtain (see Figure 6.9). With greater molecular mixing already present before reshock, the reshock event amplifies this scrambling by depositing additional vorticity over a wider range of scales, allowing the thin curtain to reach a higher asymptotic value of \bar{m} than the two thicker curtains rely more on the reshock to scramble the mixing structure, because the interactions between the interfaces are weaker.

As the shock passes through the curtain, it compresses the curtain width. This explains the negative curtain width growth that occurs for all cases. Notice that the duration of this negative curtain growth is proportional to the initial curtain width. Once the downstream

interface is reshocked, it causes the downstream interface's speed to become less positive, and possibly negative (depending on shock strength). This leads to the upstream and downstream interfaces becoming closer in space to one another, thus resulting in a decrease in curtain width despite perturbation growth occurring still on both interfaces, with more rapid perturbation growth occurring on the downstream interface due to re-shock [9]. Therefore, a greater initial curtain width increases the duration of time that the distance between upstream and downstream interfaces decreases, leading to a longer period of negative curtain growth during reshock. This negative curtain growth ceases once the upstream interface is re-shocked, imparting roughly the same interface speed to the upstream interface that was imparted to the downstream interface upon re-shock (there are slight differences in interface speeds due to slight differences in shock speeds that each interface experiences [30]).

Despite a high variation in negative curtain growth duration, the post-reshock curtain growth rate is not a strong function of initial curtain width for the cases defined in Table 6.4. It is unclear if this insensitivity is a fundamental characteristic of single mode gas curtains, or is due to the initial perturbations defined in Table 6.4. To distinguish the two, additional single-mode cases were defined with much larger wavelengths. The cases are plotted below in Figure 6.17.

Table 6.10: **Additional Single Mode Thickness Study Test Cases.**

| Case | M_s | P_1 [Pa] | T_1 [K] | a_0 [mm] | λ_0 [mm] | w_0 [mm] | $X=$ |
|---------|-------|------------|-----------|------------|------------------|------------|------|
| SM-7-1 | 1.2 | 101,325 | 300 | 1.0 | 10 | 1 | 256 |
| SM-7-6 | 1.2 | 101,325 | 300 | 1.0 | 10 | 6 | 256 |
| SM-7-24 | 1.2 | 101,325 | 300 | 1.0 | 10 | 24 | 256 |

It is clear from Figure 6.17 that the post-reshock curtain growth is proportional to the curtain's initial width. Intuitively, increasing the curtain width allows the perturbations of each interface to grow more independently. Additionally, the thin curtain's interfaces must compete to entrain the limited amount of heavy fluid into their perturbation growths, restricting the overall growth of the curtain's structure.

Figure 6.17: Single-Mode Curtain Thickness Study for large-wavelength curtains defined in Table 6.10.

This result suggests that the insensitivity observed in Figure 6.16 is most likely due to the small wavelengths cases SM-A through SM-H have. While the initial thickness effected the growth of case SM-A after initial shock passage (see Figure 6.7a), the growths of the bubbles and spikes are suffocated at later times due to the cases' small wavelengths. Therefore, upon reshock, cases varying in thickness while all sharing the small wavelength, show similar growth rates because the limitations of the wavelength overwhelm any effects of curtain thickness on the post reshock growth.

Contour Plots of Case SM-7-1 and SM-7-6 after initial shock passage are shown below to study the mechanisms behind the differences in structure width growth.

(a) SM-7-6: $t_0^+ = 0$ s

(b) SM-7-6: $t_0^+ = 100$ s

(c) SM-7-1: $t_0^+ = 0$ s

(d) SM-7-1: $t_0^+ = 100$ s

Figure 6.18: Contour plots df_z $\frac{\text{rad}}{\text{s}}$ for cases SM-7-6 (TOP) and SM-7-1 (Bottom) after initial shock passage.

Unlike the complicated initial condition cases (SM-A through SM-H), the vortex-pair structures are clearly not scrambled for Cases SM-7-1 and SM-7-6. However, notice the substantial size difference between the curtain's later-time vortex pair structures. The thin curtain's mushroom formation on the downstream side has been pulled towards the center of the curtain due to its close proximity to the upstream interface. Notice that the thin curtain's downstream interface is convex, whereas the thicker curtain's interface has become concave. This is further indication that the interface's perturbations are competing with one another to grow through entrainment. Because the downstream interface's perturbation must be in phase before it develops a mushroom-structure, the upstream perturbation has a

"head-start" on development, entraining more of the heavy fluid towards the upstream side of the curtain. This "head-start" has led to the downstream interface's convex shape. With only a finite amount of heavy fluid available for entrainment, the thin curtain's vortices begin to entrain the surrounding air in the development of the mushroom structure, diminishing the structure growth while increasing the mixedness of the curtain. This can be seen in the SF₆ contour plots for the two cases, pictured in Figure 6.19. The thin curtain's "tails" are in a well-mixed state due to this phenomena. Furthermore, notice that most of the fluid has been drawn towards the upstream (left) side of the thin curtain's perturbations.

(a) SM-7-6: $t_0^+ = 0$ s

(b) SM-7-6: $t_0^+ = 100$ s

(c) SM-7-1: $t_0^+ = 0$ s

(d) SM-7-1: $t_0^+ = 100$ s

Figure 6.19: Contour plots of SF₆ for cases SM-7-6 (TOP) and SM-7-1 (Bottom) after initial shock passage.

6.2.3 Multi-Mode Curtain Reshock Studies

Cases MM-2 and MM-8 were run under re-shock conditions to understand how the multi-modal shape of the gas curtain affects the post-reshock curtain growth, plotted in Figure 6.20a.

(a) (b)

Figure 6.20: Multi-Mode Gas Curtain Post-Reshock Growth and Results for cases differing in shape (Equation 6.2).

The late-time molecular mixing, shown in Figure 6.20b, is insensitive to changes in the number of modes, because the re-shock event sufficiently redistributes vorticity to the point that a similar mixed state is eventually reached by both cases.

Figure 6.20a indicates that an increase in the number of initial modes leads to a slight decline in post-reshock growth rates of the structure, due to the higher degree of modal competition. This behavior is consistent with the post-reshock growth rate behavior for multi-mode single-interface RMI configurations [9], and contradicts the findings of [31]. Applying [9]'s randomness factor characterization for single-interface RMIs to the cases defined in Table 6.7, it can be seen in Table 6.11 that the characterization holds for the reshock structure width growth rates $\frac{dW_R}{dt}$ of gas curtains as well (if the curtain width is held fixed at a sufficiently large value).

The evolution of cases MM-2 and MM-8 can be seen in Figure 6.21. Adding more

Table 6.11: [9]'s characterization applied to multi-modal gas curtains.

| Case | a_0 [mm] | k_{\max} | $R = \frac{a_0 k_{\max}}{L_y}$ | $\frac{dW_R}{dt}$ |
|------|------------|------------|--------------------------------|-------------------|
| MM-2 | 0.5 | 2 | 0.01 | 17.76 |
| MM-8 | 0.5 | 8 | 0.04 | 9.23 |

(a) MM-2 before reshock. (b) MM-2: $t_R^+ = 0$ s (c) MM-2: $t_R^+ = 100$ s

(d) MM-8 before reshock. (e) MM-8: $t_R^+ = 0$ s (f) MM-8: $t_R^+ = 100$ s

Figure 6.21: Contour plots of γ_{SF_6} for cases MM-2 (TOP) and MM-8 (Bottom) after reshock.

modes to the initial perturbations of the curtain's interfaces increases the modal competition between vortices deposited upon shock passage, restricting the bubble and spike growth before reshock. Furthermore, the modal competition increases the transverse momentum of the bubble and spikes at the expense of their stream-wise momentum [9]. With smaller, transversely oriented bubbles and spikes present at reshock, the additional energy deposited by reshock redistributes the vorticity over fewer scales, and increases the transverse momentum of the structures. Furthermore, the increased modal competition, present in the higher mode case, causes the curtain's interfaces to reach a more random state prior to reshock [9]. The more random perturbations present at reshock inhibit the additional energy (from

reshock) from resulting in structure growth, due to the random velocity/vorticity field that is only further scrambled due to reshock [7, 9, 20]. This behavior is well-understood because it occurs in single-interface RMIs as well [9, 45, 20]. It seems that the interactions between interfaces at the currently defined curtain thicknesses ($w_0 = 6$ mm) are too weak to affect this behavior. Following the logic and understanding gained thus far about the effects of initial curtain thickness, it is reasonable to expect that at a sufficiently thin the interactions between the curtain's interfaces will overwhelm the modal competition behavior occurring on MM-2's and MM-8's interfaces, resulting in comparable post-reshock mixing layer growth rates that are independent of the initial number of modes. To test this hypothesis, two additional cases were defined that change the multi-modal initial thickness to 1 mm (Table 6.12).

Table 6.12: Multi-Mode Thin Curtain Definitions.

| Case | M_s | P_1 [Pa] | T_1 [K] | # of Modes | a_0 [mm] | w_0 [mm] | w_0 [mm] |
|--------|-------|------------|-----------|------------|------------|------------|------------|
| MM-2-1 | 1.5 | 101,325 | 300 | 2 | 0.50 | 5 = 18 | 1 |
| MM-8-1 | 1.5 | 101,325 | 300 | 8 | 0.50 | 5 = 18 | 1 |

The resulting structure width growths for cases defined in Table 6.12 are plotted in Figure 6.22.

Figure 6.22 shows that the thin curtains, despite having a differing number of initial modes, share the same post-reshock growth rate. As hypothesized, for sufficiently thin curtains, the strong interactions between the curtain's interfaces scramble the vortex pair structures and inhibit the growth of bubbles and spikes. Furthermore, Case MM-2-1 experiences slower perturbation growth (compared to MM-2) due to the limited amount of heavy fluid available to feed the entrainment process. Comparing the structures of cases MM-2 (Figure 6.21) and MM-2-1 (Figure 6.23) shows that, in the thin curtain, interface interactions have disrupted the bubble and spike growth, largely inhibiting the entrainment process. Notice that at comparable times, both MM-2-1 and MM-8-1 are much more molecularly-mixed compared to MM-2 and MM-8, respectively. With less fluid avail-

Figure 6.22: Structure Width versus time for Cases defined in Table 6.12.

able, the developing structures gather more air into the bubble and spike growth, leading to a more mixed state achieved in the bubbles and spikes compared to the thicker curtains. The vortex-tube-merger process, shown in Figure 6.9, also concentrates vortex structures in the middle of the curtain and breaks down the vortex pairing, such that the vortices lead to mixing of species rather than structure growth.

(a) MM-2-1 before reshock. (b) MM-2-1: $t_R^+ = 0$ s (c) MM-2-1: $t_R^+ = 100$ s

(d) MM-8-1 before reshock. (e) MM-8-1: $t_R^+ = 0$ s (f) MM-8-1: $t_R^+ = 100$ s

Figure 6.23: Contour plots α_{SF_6} for cases MM-2-1 (TOP) and MM-8-1 (Bottom) after reshock. t_R^+ represents time after reshock.

6.2.4 Multi-Mode Curtain Thickness Reshock Studies

The 2-mode and 8-mode cases with varying initial curtain thicknesses were run under reshock conditions to further investigate the thickness effects on multi-modal gas curtain's post-reshock behavior. Results are plotted in Figure 6.24.

From Figure 6.24 it can be seen that, generally, a decrease in initial thickness leads to a decrease in the post reshock structure growth of the curtain. Notice, however, that cases MM-2-24 and MM-2 share similar growth rates, whereas case MM-8-24 has a slightly higher growth rate than case MM-8. Based on the previous discussion, this suggests that both the 6 mm and 24 mm curtains are sufficiently thick to the point where the interactions between interfaces for the MM-2 cases have little effect on the post-reshock growth rate. However, the change in curtain thickness between MM-8 and MM-8-24 is enough to effect

Figure 6.24: Multi-Mode Gas Curtain Post-Reshock Growth for (a) MM-2 and (b) MM-8 cases.

Figure 6.25: Multi-Mode Gas Curtain for (a) MM-2 and (b) MM-8 cases.

the growth rates of the 8-mode cases. This comparison indicates that the effect of initial curtain thickness on the post reshock growth rate is not universal, but dependent on the curtain's initial perturbations.

Results for (Figure 6.25) show that the degree of mixedness is significantly influenced by the initial thickness of the curtain, and relatively insensitive to the initial number of modes present in the curtain. Notice that the thin (1 mm) curtains have a significantly higher late-time value than the 6 mm and 24 mm curtains, further solidifying the claim that curtain thickness and are inversely related. The relationship does appear to be somewhat asymptotic (suggested by single-mode results as well), where increasing curtain thickness

beyond a certain point does not result in further decline. Thinning the curtain results in stronger vortex interactions between the curtain's interfaces, leading to the vortices acting to mix the species rather than grow the mixing layer.

6.2.5 Effect of Random Fluctuations

Random fluctuations were added to the initial interface perturbations of case MM-2 in order to see the effect of such fluctuations on the post-reshock growth rate of the gas curtain, plotted in Figure 6.26. From Figure 6.26, it can clearly be seen that the addition of ran-

Figure 6.26: Gas curtain growth (a) and (b), showing the effects of random fluctuations on the post-reshock growth rate.

dom fluctuations significantly diminishes the post-reshock structure width growth. Random fluctuations lead to greater redistribution of vorticity upon reshock (due to more randomness in the density gradient across perturbations) and more lateral motion of the bubbles and spikes [20]. This greater redistribution of vorticity acts to scramble the perturbations

more severely, reducing the post-reshock growth of the curtain. This behavior is exhibited in single-interface RMI as well, and supports [9]'s "randomness" characterization discussed previously (if the curtain thickness is fixed to a sufficiently large value).

6.3 Discussion of Applicability

Several ad hoc decisions had to be made at the very beginning of the simulation process. The initial amplitude, wavelength, and curtain thickness choices were informed decisions based on single-interface RMIs [9] and gas curtains [4, 31, 8] studies previously performed. However, the selections of the parameters at some level were arbitrary in nature. From the results discussed above, it is clear that the sensitivity of the post-reshock growth to changes in initial curtain thickness depends on the combination of initial conditions as a whole. Therefore, care must be taken when applying or extrapolating the results discussed above to a new physical set-up. While the trends are fundamentally sound, at what point interactions between interfaces become important is entirely dependent on the problem at hand.

Furthermore, this study was limited to gas curtains whose interfaces were in-phase with one another. The instability becomes more complex if the interface perturbations are out of phase. Most likely, in this scenario the scrambling of the vortex-pair structures will become more dominant (given the curtain thickness is sufficiently small), because the vorticity generated on each interface will no longer be guaranteed to have an oppositely-signed counterpart on the opposing interface, leading to easier vortex merging at earlier times between the interfaces.

Additionally, this study was performed using two-dimensional simulations. In three dimensions, the vortex stretching mechanism shown in Equation 2.1 becomes activated. It is well-known that this mechanism is responsible for the energy cascade in turbulent flows, stretching vortex filaments such that large scale structures are sheared into smaller structures. [9] showed that vortex stretching can possibly strengthen the vorticity if the

vortex rings (that form the bubbles and spikes in three-dimensions) are stretched. Furthermore, three-dimensional bubbles and spikes have a point contact with the shock, whereas in two-dimensions the contact is a line. These two phenomena are known to cause three-dimensional single-interface RMIs to have larger growth rates compared to two-dimensional simulations. Extrapolating this result to gas curtains, it is logical to think that interface interactions will become more prevalent in three-dimensions, as greater growth rates indicate that the vortex structures developing on the curtain's interfaces in three-dimensions will interact sooner in time. This is merely speculation however, and must be tested rigorously.

CHAPTER 7

CONCLUSIONS

7.1 Summary

The main purpose of this thesis was to understand the behavior of gas curtain instabilities post-reshock. Several objectives were identified in Chapter 3.

In order to meet these objectives, the simulation set-up of the current work was verified by matching first empirical models [14] and past numerical results [9] for a single-interface RMI, and then by matching both experimental [8, 31] and numerical [4, 7] results for gas curtain instabilities. Then, several initial curtain configurations were defined and their behaviors to a single shock passage were studied and shown to be in agreement with past studies [4, 8, 31, 33].

With the gas curtain behavior to a single shock validated and understood, the same cases were simulated in re-shock conditions to investigate the sensitivity of the gas curtain's post-reshock behavior to changes in initial shape (both single- and multi-mode) and thickness of the curtain. The behavior was quantified using two measures: (1) the structure width measure widely used in past studies ([4, 8, 30, 31, 7, 33]), and (2) through novel calculations of molecular mixing fraction which have not been performed by previous studies of gas curtains.

It was found that the post-reshock curtain growth-rate is sensitive to the initial conditions, suggesting that memory of the initial conditions is retained post-reshock for a gas curtain. If the curtain thickness is sufficiently thin, the interactions between the curtain's interfaces significantly impede the growth of perturbations on either interface, leading to a reduction in the curtain's structure width growth post-reshock. With a limited amount of heavy fluid present in the domain, the thin curtain's interfaces compete to entrain the

heavy fluid into the development of their perturbations. Furthermore, the interfaces draw more light fluid into their developing perturbations and the curtain itself, increasing the mixed-ness of the curtain while stifling structure width growth. If the initial interface perturbations are complex, the interface interactions disrupt the vortex-pair structures such that the present vorticity induces rapid mixing of species within the curtain, resulting in the thinner curtains reaching a greater state of mixed-ness at late times after reshock. Additionally, these effects of curtain thickness are amplified by the many wave reverberations traveling through the structure width, redistributing vorticity even further. This result is significant, especially for reacting flows, because it indicates that faster combustion (or afterburning in an explosion) could be reached with the thinning of the gas curtain in flow systems.

7.2 Future Work

This thesis provides basic understandings of gas curtain instabilities experiencing reshock. However, the analysis of the extremely complex physics occurring in such problems is still in its infancy and more investigations are recommended for future studies. The key recommendations for future work are:

1. The effects of curtain thickness on the post-reshock growth of the curtain have been shown to depend on the initial shape conditions of the curtain. Further analysis should be performed in order to properly quantify this dependence, such that the effects of curtain thickness can be predicted based on the initial shape of the curtain's perturbations.
2. While two-dimensional analysis provides a strong foundational understanding of gas curtain instabilities, it is recommended to extend this investigation into three-dimensional simulations, making it much more representative of physical scenarios. It is well known that vortex stretching plays an integral role in the development of

turbulence, and that turbulence can only "exist" in three dimensions, therefore it is very important that the understanding of gas curtain instabilities be extended to three-dimensions.

3. Due to the specific application of gas curtain instabilities in explosive blasts, the study of curtain instabilities should be extended into multi-phase studies. During explosive blasts, curtains of detonation products develop in the presence of solid particles that also result from the destructive nature of the blast. Multi-phase RMI studies [20] have indicated that the presence of solid particles have a significant impact on the perturbation growth, so it is likely that the presence of solid particles will impact curtain instabilities as well.
4. Following #2, the study of curtain instabilities should be extended into reacting flow conditions, providing more physical understanding of explosive events.

REFERENCES

- [1] K. Balakrishnan, F. Genin, D. V. Nance, and S. Menon, "Numerical Study of Blast Characteristics from Detonation of Homogeneous Explosives Shock Waves, vol. 20, no. 2, pp. 147–162, 2010.
- [2] E. Fedina, K. C. Gottiparthi, C. Fureby, and S. Menon, "Combustion in Afterburning Behind Explosive Blasts, Coarse Grained Simulation and Turbulent Mixing, pp. 393, 2016.
- [3] J. C. Schulz, "A study of magnetoplasmadynamic effects in turbulent supersonic flows with application to detonation and explosion, Georgia Tech Theses and Dissertations, 2015.
- [4] A. Gowardhan and F. Grinstein, "Numerical simulation of richtmyer–meshkov instabilities in shocked gas curtains, Journal of Turbulence, no. 12, N43, 2011.
- [5] R. Baltrusaitis, M. Gittings, R. Weaver, R. Benjamin, and J. Budzinski, "Simulation of shock-generated instabilities, Physics of Fluids, vol. 8, no. 9, pp. 2471–2483, 1996.
- [6] K. O. Mikaelian, "Turbulent mixing generated by rayleigh-taylor and richtmyer-meshkov instabilities, Physica D: Nonlinear Phenomena, vol. 36, no. 3, pp. 343–357, 1989.
- [7] S. K. Shankar and S. K. Lele, "Numerical investigation of turbulence in reshocked richtmyer–meshkov unstable curtain of dense gas, Shock Waves, vol. 24, no. 1, pp. 79–95, 2014.
- [8] B. Balakumar, G. Orlicz, C. Tomkins, and K. Prestridge, "Simultaneous particle-image velocimetry–planar laser-induced fluorescence measurements of richtmyer–meshkov instability growth in a gas curtain with and without reshock, Physics of Fluids, vol. 20, no. 12, p. 124 103, 2008.
- [9] S. Ukai, K. Balakrishnan, and S. Menon, "Growth Rate Predictions of Single-and Multi-mode Richtmyer–Meshkov Instability With Reshock, Shock Waves, vol. 21, no. 6, p. 533, 2011.
- [10] Y. Zhou et al., "Rayleigh–Taylor and Richtmyer-Meshkov Instabilities: A Journey Through Scales, Physica D: Nonlinear Phenomena, p. 132 838, 2021.
- [11] S.-I. Sohn, "Bubble interaction model for hydrodynamic unstable mixing, Physical Review E, vol. 75, no. 6, p. 066 312, 2007.

- [12] R. D. Richtmyer, “Taylor Instability in Shock Acceleration of Compressible Fluids,” Los Alamos Scientific Lab., N. Mex., Tech. Rep., 1954.
- [13] R. L. Holmes, J. W. Grove, and D. H. Sharp, “Numerical Investigation of Richtmyer–Meshkov Instability Using Front Tracking,” *Journal of Fluid Mechanics*, vol. 301, pp. 51–64, 1995.
- [14] O. Sadot *et al.*, “Study of Nonlinear Evolution of Single-Mode and Two-Bubble Interaction Under Richtmyer-Meshkov Instability,” *Physical Review Letters*, vol. 80, no. 8, p. 1654, 1998.
- [15] K. O. Mikaelian, “Explicit Expressions for the Evolution of Single-Mode Rayleigh-Taylor and Richtmyer-Meshkov Instabilities at Arbitrary Atwood Numbers,” *Physical Review E*, vol. 67, no. 2, p. 026 319, 2003.
- [16] V. Goncharov, “Analytical Model of Nonlinear, Single-Mode, Classical Rayleigh-Taylor Instability at Arbitrary Atwood Numbers,” *Physical Review Letters*, vol. 88, no. 13, p. 134 502, 2002.
- [17] K. O. Mikaelian, “Rayleigh–taylor and richtmyer–meshkov instabilities in finite-thickness fluid layers,” *Physics of Fluids*, vol. 7, no. 4, pp. 888–890, 1995.
- [18] C. Niederhaus and J. W. Jacobs, “Experimental study of the richtmyer–meshkov instability of incompressible fluids,” *Journal of Fluid Mechanics*, vol. 485, pp. 243–277, 2003.
- [19] Q. Zhang and S.-I. Sohn, “An analytical nonlinear theory of richtmyer-meshkov instability,” *Physics Letters A*, vol. 212, no. 3, pp. 149–155, 1996.
- [20] S. Ukai, *Richtmyer meshkov instability with reshock and particle interactions*, 2010.
- [21] B. Collins and J. Jacobs, “PLIF Flow Visualization and Measurements of the Richtmyer–Meshkov Instability of an Air/SF6 Interface,” *Journal of Fluid Mechanics*, vol. 464, pp. 113–136, 2002.
- [22] C. Long, V. Krivets, J. Greenough, and J. Jacobs, “Shock Tube Experiments and Numerical Simulation of the Single-Mode, Three-Dimensional Richtmyer–Meshkov Instability,” *Physics of Fluids*, vol. 21, no. 11, p. 114 104, 2009.
- [23] J.-s. Bai, B. Wang, T. Wang, and K. Liu, “Numerical Simulation of the Richtmyer-Meshkov Instability in Initially Nonuniform Flows and Mixing with Reshock,” *Physical Review E*, vol. 86, no. 6, p. 066 319, 2012.
- [24] M. Vetter and B. Sturtevant, “Experiments on the Richtmyer-Meshkov Instability of an Air/SF6 Interface,” *Shock waves*, vol. 4, no. 5, pp. 247–252, 1995.

- [25] E. Leinov *et al.*, “Experimental and Numerical Investigation of the Richtmyer–Meshkov Instability Under Re-shock Conditions,” *Journal of Fluid Mechanics*, vol. 626, pp. 449–475, 2009.
- [26] B. Thornber, D. Drikakis, D. Youngs, and R. Williams, “Growth of a richtmyer-meshkov turbulent layer after reshock,” *Physics of Fluids*, vol. 23, no. 9, p. 095 107, 2011.
- [27] G. I. Taylor, “The instability of liquid surfaces when accelerated in a direction perpendicular to their planes. i,” *Proceedings of the Royal Society of London. Series A. Mathematical and Physical Sciences*, vol. 201, no. 1065, pp. 192–196, 1950.
- [28] E. Ott, “Nonlinear evolution of the rayleigh-taylor instability of a thin layer,” *Physical Review Letters*, vol. 29, no. 21, p. 1429, 1972.
- [29] J. Jacobs, D. Jenkins, D. Klein, and R. Benjamin, “Experimental study of instability growth patterns of a shock-accelerated, thin fluid layer,” Los Alamos National Lab., NM (United States), Tech. Rep., 1993.
- [30] J. M. Budzinski, R. F. Benjamin, and J. W. Jacobs, “Influence of initial conditions on the flow patterns of a shock-accelerated thin fluid layer,” *Physics of Fluids*, vol. 6, no. 11, pp. 3510–3512, 1994.
- [31] S. Balasubramanian, G. Orlicz, and K. Prestridge, “Experimental Study of Initial Condition Dependence on Turbulent Mixing in Shock-Accelerated Richtmyer–Meshkov Fluid Layers,” *Journal of Turbulence*, vol. 14, no. 3, pp. 170–196, 2013.
- [32] A. A. Gowardhan, J. R. Ristorcelli, and F. F. Grinstein, “The bipolar behavior of the richtmyer–meshkov instability,” *Physics of fluids*, vol. 23, no. 7, p. 071 701, 2011.
- [33] K. O. Mikaelian, “Numerical simulations of richtmyer–meshkov instabilities in finite-thickness fluid layers,” *Physics of Fluids*, vol. 8, no. 5, pp. 1269–1292, 1996.
- [34] J. Jacobs, D. Jenkins, D. Klein, and R. Benjamin, “Nonlinear growth of the shock-accelerated instability of a thin fluid layer,” *Journal of Fluid Mechanics*, vol. 295, pp. 23–42, 1995.
- [35] F. Génin and S. Menon, “Studies of shock/turbulent shear layer interaction using large-eddy simulation,” *Computers & Fluids*, vol. 39, no. 5, pp. 800–819, 2010.
- [36] A. Harten, P. D. Lax, and B. v. Leer, “On upstream differencing and godunov-type schemes for hyperbolic conservation laws,” *SIAM review*, vol. 25, no. 1, pp. 35–61, 1983.

- [37] B. Einfeldt, “On godunov-type methods for gas dynamics,” *SIAM Journal on numerical analysis*, vol. 25, no. 2, pp. 294–318, 1988.
- [38] B. Einfeldt, C.-D. Munz, P. L. Roe, and B. Sjögreen, “On godunov-type methods near low densities,” *Journal of computational physics*, vol. 92, no. 2, pp. 273–295, 1991.
- [39] F. Génin and S. Menon, “Simulation of turbulent mixing behind a strut injector in supersonic flow,” *AIAA journal*, vol. 48, no. 3, pp. 526–539, 2010.
- [40] R. J. LeVeque *et al.*, *Finite volume methods for hyperbolic problems*. Cambridge university press, 2002, vol. 31.
- [41] G. L. Bryan, M. L. Norman, J. M. Stone, R. Cen, and J. P. Ostriker, “A piecewise parabolic method for cosmological hydrodynamics,” *Computer physics communications*, vol. 89, no. 1-3, pp. 149–168, 1995.
- [42] E. F. Toro, M. Spruce, and W. Speares, “Restoration of the contact surface in the hll-riemann solver,” *Shock waves*, vol. 4, no. 1, pp. 25–34, 1994.
- [43] Y. Zhou, “Rayleigh–taylor and richtmyer–meshkov instability induced flow, turbulence, and mixing. ii,” *Physics Reports*, vol. 723, pp. 1–160, 2017.
- [44] W. H. Cabot and A. W. Cook, “Reynolds number effects on rayleigh–taylor instability with possible implications for type ia supernovae,” *Nature Physics*, vol. 2, no. 8, pp. 562–568, 2006.
- [45] B. Thornber *et al.*, “Late-time growth rate, mixing, and anisotropy in the multimode narrowband richtmyer–meshkov instability: The -group collaboration,” *Physics of fluids*, vol. 29, no. 10, p. 105 107, 2017.
- [46] Y. Zhou, W. H. Cabot, and B. Thornber, “Asymptotic Behavior of the Mixed Mass in Rayleigh–Taylor and Richtmyer–Meshkov Instability Induced Flows,” *Physics of Plasmas*, vol. 23, no. 5, p. 052 712, 2016.
- [47] L. Brandt, T. Cichocki, and K. Nomura, “Asymmetric vortex merger: Mechanism and criterion,” *Theoretical and Computational Fluid Dynamics*, vol. 24, no. 1, pp. 163–167, 2010.